

# Quantum-accelerated conjugate gradient methods via spectral initialization

Shigetora Miyashita<sup>1,\*</sup> and Yoshi-aki Shimada<sup>1,†</sup>

<sup>1</sup>*Research Institute of Advanced Technology, SoftBank Corp.,  
Tokyo Portcity Takeshiba Office Tower 1-7-1, Kaigan, Minato-ku, Tokyo, 105-7529, Japan*

(Dated: February 11, 2026)

Solving large-scale linear systems problems is a central task in scientific and industrial computing. Classical iterative solvers face increasing difficulty as the number of unknowns becomes large, while fully quantum linear solvers require fault-tolerant resources that remain far beyond near-term feasibility. Here we propose a quantum-accelerated conjugate gradient (QACG) framework in which a fault-tolerant quantum algorithm is used exclusively to construct a spectrally informed initial guess for a classical conjugate gradient (CG) solver. Rather than replacing classical kernels, the quantum subroutine functions as a cooperative accelerator that selectively suppresses low-energy spectral components responsible for slow classical convergence. We analyze the total runtime and resource requirements of this integrated quantum-HPC platform for the 3D Poisson equation. A central feature of QACG is a controllable decomposition of the condition number between the quantum and the classical solver, enabling flexible allocation of computational effort across quantum and classical resources. Under explicit architectural assumptions, we identify regimes in which this cooperative strategy yields a runtime advantage over purely classical approaches while requiring substantially fewer quantum resources than end-to-end quantum linear solvers. These results illustrate a concrete pathway toward the scientific and industrial use of early-stage fault-tolerant quantum computing and point to a scalable hybrid paradigm in which quantum devices act as accelerators within high-performance computing workflows rather than as standalone replacements.

## I. INTRODUCTION

Quantum algorithms present a unique path for computation by introducing a set of elementary building blocks, based on unitary operations acting on quantum states, that can be used to accelerate specific computational tasks. From this perspective, quantum computation is not intended to replace classical algorithms. Rather, it enables efficient solutions to specific problems that are prohibitively costly in the classical setting, by exploiting physical phenomena such as superposition and entanglement. This perspective traces back to Feynman's insight that quantum dynamics cannot be efficiently simulated using classical resources alone [1], demonstrating that quantum mechanics enable information processing that lie beyond the reach of classical computation. Subsequent developments, most notably Shor's factoring algorithm [2–4] and Grover's search algorithm [5, 6], showed that carefully designed quantum subroutines can be embedded within larger computational workflows to achieve substantial performance gains. More recently, advances in quantum error correction [7–10] have elevated this paradigm into a rigorous theoretical framework, enabling a systematic assessment of quantum computation. These developments have reshaped the boundary between classical and quantum computation and delineated the regimes in which quantum advantage may arise.

Recent attention has shifted toward noisy intermediate-scale quantum (NISQ) devices [11],

which operate without full error correction. In this regime, collaborative quantum-classical algorithms, such as quantum-selected configuration interaction (QSCI) [12] and sample-based quantum diagonalization (SQD) [13, 14], have enabled practical applications including the estimation of molecular ground-state energies. When embedded in workflows supported by high-performance computing (HPC) resources, these methods have extended simulations beyond the memory limits of purely classical architectures. In parallel, fault-tolerant quantum computing (FTQC) [15–18] offers provably correct solutions to selected quantum chemistry problems. For example, few-qubit demonstrations of quantum phase estimation (QPE) [19] have produced certified ground-state energies. Because QPE also appears as a subroutine in a broad range of algorithms including the Harrow–Hassidim–Lloyd (HHL) algorithm [20], its relevance extends across physics, chemistry, and engineering.

Despite this progress, both paradigms face substantial limitations. In NISQ-based quantum-centric workflows, it remains unclear if quantum resources can provide a guaranteed advantage in general tasks. Problem-specific techniques, such as the local unitary cluster Jastrow (LUCJ) ansatz [21], achieve impressive results in electronic structure calculations but do not readily generalize. Conversely, many FTQC-oriented proposals restrict the role of classical HPC to auxiliary preprocessing or postprocessing tasks [22]. Although error correction is indispensable for large-scale quantum computation, existing demonstrations have not yet addressed industrial-scale problems end to end. Taken together, these observations suggest that neither classical HPC nor near-term or fault-tolerant quantum computing alone can ef-

\* [shigetora.miyashita@g.softbank.co.jp](mailto:shigetora.miyashita@g.softbank.co.jp)

† [yoshiaki.shimada01@g.softbank.co.jp](mailto:yoshiaki.shimada01@g.softbank.co.jp)

ficiently address the full spectrum of large-scale scientific and industrial workloads. Classical HPC struggles with problems dominated by severe ill-conditioning or extreme spectral complexity, while quantum algorithms applied monolithically often incur prohibitive resource requirements.

These considerations motivate a central question: does there exist a computational regime beyond monolithic architectures, whether purely classical or purely quantum, that can deliver measurable and practically relevant benefits? In this work, we use the term *beyond monolithic architecture* to denote a setting in which classical and quantum resources are combined within an integrated quantum–HPC system, each addressing the aspects of a problem for which it is best suited, without claiming universal or unconditional advantage.

The objective of this study is to quantitatively identify the conditions under which such a regime can be realized for large-scale linear systems. We propose an integrated fault-tolerant quantum–HPC algorithm in which the HHL algorithm is used to construct a spectral initial guess for the classical conjugate gradient (CG) method. The quantum subroutine is restricted to a low-energy spectral subspace that is responsible for slow classical convergence, while the classical HPC solver performs the bulk of the numerical workload. In this workflow, the quantum component mitigates the most ill-conditioned modes, and the classical CG iteration exploits its scalability in the remaining subspace. As a result, the effective condition number governing the quantum stage is reduced, and the total number of classical floating-point operations is correspondingly lowered for problems with a large number of unknowns  $N$ .

We analyze the performance of this integrated quantum–HPC system using explicit gate-complexity and runtime models. The quantum component is evaluated within a partially fault-tolerant framework based on the STAR architecture [23], while the classical component is modeled on a contemporary HPC platform. Importantly, our analysis does not assume idealized end-to-end quantum acceleration; rather, it treats the method as a cooperative workflow whose advantage is conditional on problem structure, spectral properties, and architectural parameters.

This perspective aligns with increasing interest in quantum–HPC integration, where quantum processors are incorporated into existing HPC environments as specialized accelerators [24, 25]. While such integration enables realistic assessments of hybrid workflows, the classes of applications that can benefit, and the nature of those benefits, remain open questions.

Focusing on computer-aided engineering (CAE), an industrially important domain dominated by large sparse linear systems, we present a quantum-accelerated conjugate gradient (QACG) method as a concrete case study. By demonstrating a conditional performance advantage for a representative CAE problem, this work illustrates how cooperation between quantum and classical

resources can expand the range of tractable computations beyond what is achievable with either paradigm in isolation.

The remainder of this paper is organized as follows. In Sec. II, we review the linear systems problem and the relevant classical and quantum algorithms, emphasizing their computational complexity. In Sec. III, we introduce the QACG workflow and present an explicit quantum circuit for a three-dimensional Poisson equation. In Sec. IV, we develop time-complexity models for CG, HHL, and QACG, assuming a contemporary HPC platform and a STAR-architecture quantum device with representative parameters such as the quantum error correction (QEC) cycle times. In Sec. V, we report runtime and resource estimates in terms of logical qubit counts and gate complexity as well as the numerical simulation to demonstrate the effectiveness of our approach. We conclude in Sec. VI with a discussion of implications, limitations, and open challenges.

## II. BACKGROUND

A primary focus of this work is the solution of large-scale systems of linear equations of the form

$$Ax = b, \quad (1)$$

where  $A$  is a sparse Hermitian matrix and  $b$  is a given right-hand-side vector. Such linear systems arise ubiquitously in scientific computing, most notably through the discretization of boundary value problems governed by partial differential equations (PDEs). Applications ranging from fluid dynamics and electromagnetism to structural analysis and materials science rely on PDE models to describe spatially varying physical quantities. Discretization by finite difference, finite volume, or finite element methods yields algebraic systems whose dimension reflects the resolution of the underlying mesh. As this resolution increases, the number of unknowns  $N$  grows rapidly, leading to large and computationally demanding linear systems that often dominate the overall cost of CAE simulations on modern HPC platforms.

For linear systems of the form (1), Krylov subspace methods are the standard solvers in large-scale numerical linear algebra. Among them, CG is widely used when  $A$  is symmetric positive definite (SPD). CG can be derived from the Lanczos process by applying the Ritz–Galerkin condition to the quadratic functional

$$f(x) = \frac{1}{2}x^T Ax - b^T x, \quad (2)$$

whose minimization is equivalent to solving  $Ax = b$ . Assuming sparse matrix storage and efficient memory access, each CG iteration requires  $\mathcal{O}(N)$  operations. The number of iterations required to reach a target accuracy  $\varepsilon$  depends on the condition number  $\kappa$  of  $A$ , leading to the

overall complexity

$$\mathcal{T}_{\text{CG}} = \mathcal{O}(N\sqrt{\kappa} \log \varepsilon^{-1}). \quad (3)$$

The convergence behavior of CG follows from classical Krylov subspace theory. After  $k$  iterations, the error satisfies

$$\|e^{(k)}\|_A = \min_{p \in \mathcal{P}_k, p(0)=1} \|p(A)e^{(0)}\|_A, \quad (4)$$

where  $\mathcal{P}_k$  denotes the set of polynomials of degree at most  $k$  and  $\|v\|_A := \sqrt{v^T A v}$  is the energy norm. Choosing  $p$  from the Chebyshev family yields the classical bound [26]

$$\frac{\|e^{(k)}\|_A}{\|e^{(0)}\|_A} \leq 2 \left( \frac{\sqrt{\kappa} - 1}{\sqrt{\kappa} + 1} \right)^k, \quad (5)$$

which shows that CG convergence is governed by  $\sqrt{\kappa}$ . This dependence constitutes a fundamental bottleneck: even on large-scale HPC systems, the presence of small eigenvalues can significantly slow convergence.

A standard strategy to mitigate this bottleneck is preconditioning, which aims to reduce the effective condition number. Multiscale and multigrid methods are prominent examples. By exploiting a hierarchy of discretizations, multigrid techniques eliminate low-frequency error components on coarse grids and high-frequency components on fine grids. A generic multigrid update can be written as [27]

$$x^{(k+1)} = x^{(k)} + R_{(k)}(b - A_{(k)}x^{(k)}), \quad (6)$$

where  $R_{(k)}$  approximates the inverse of  $A_{(k)}$  at level  $k$ . Under ideal assumptions, including ellipticity, smooth coefficients, and well-defined grid hierarchies, multigrid methods can achieve an effective condition number  $\kappa = \mathcal{O}(1)$  and overall complexity  $\mathcal{O}(N)$ . In practice, however, this performance is highly problem dependent. Irregular geometries, discontinuous coefficients, or non-separable operators may prevent the construction of effective hierarchies, leading to substantial degradation in performance.

Adaptive mesh refinement (AMR) provides a complementary strategy by increasing resolution only where required. Refinement is guided by a posteriori error indicators, such as [28]

$$\frac{|x_{i+1} - 2x_i + x_{i-1}|}{|x_{i+1} - x_i| + |x_i - x_{i-1}| + \varepsilon(|x_{i+1}| + 2|x_i| + |x_{i-1}|)}, \quad (7)$$

with elements exceeding a prescribed threshold marked for refinement. Although AMR can substantially reduce the number of degrees of freedom required to achieve a target accuracy, it introduces algorithmic and implementation complexity. Dynamic data structures, irregular communication patterns, and load imbalance can limit scalability on HPC systems. Moreover, AMR relies on

assumptions about solution regularity that may fail in turbulent, strongly nonlinear, or tightly coupled multi-physics problems.

Despite the success of CG combined with multiscale or adaptive techniques, classical solvers remain constrained by the scaling of memory and iteration costs with  $N$ . In CAE applications, further refinement or more aggressive preconditioning is often impractical due to memory capacity, communication overhead, or algorithmic complexity. These limitations motivate the exploration of quantum algorithms that may address specific spectral bottlenecks in large-scale linear solvers.

QLSA [29, 30] aims to prepare a quantum state proportional to the solution of the linear system (1),

$$|x\rangle = \frac{A^{-1}|b\rangle}{\|A^{-1}|b\rangle\|}, \quad (8)$$

rather than explicitly outputting the solution vector. This formulation illustrates a key distinction from classical solvers such as CG. While CG produces a solution with a runtime that scales linearly in the problem size  $N$  as presented by (3), QLSA target a quantum state representation whose preparation cost depends only logarithmically on  $N$ . In this sense, QLSA offer an exponential improvement in the dependence on system size  $N$ .

This advantage, however, must be weighed against the dependence on the condition number  $\kappa$ . Classical CG converges in a number of iterations proportional to  $\sqrt{\kappa}$ , making it highly effective for well-conditioned or moderately conditioned problems. By contrast, quantum algorithms face a dependence on  $\kappa$  and the target precision  $\varepsilon$ , shifting the computational bottleneck from system size to spectral properties.

Within the family of QLSA, the original HHL algorithm [20] and later refinements achieve different trade-offs between these parameters. In terms of query or gate complexity, HHL scales as

$$\mathcal{G}_{\text{HHL}} = \mathcal{O}(\log N \kappa^2 \varepsilon^{-1}), \quad (9)$$

while more modern QLSA formulations based on block-encoding and quantum singular value transformation achieve the improved scaling [31]

$$\mathcal{Q}_{\text{QLSA}} = \mathcal{O}(\log N \kappa \log \varepsilon^{-1}). \quad (10)$$

The latter represents a significant theoretical improvement, reducing the quadratic dependence on  $\kappa$  to linear and improving the precision dependence from polynomial to logarithmic.

Despite this asymptotic advantage, the dependence on  $\kappa$  remains a central challenge for quantum solvers, particularly for the ill-conditioned systems commonly encountered in CAE. In such settings, the condition number often grows rapidly with problem size, offsetting the exponential improvement in  $N$  and limiting the practical applicability of fully quantum approaches.

As in classical numerical linear algebra, precondition-

ing therefore plays a crucial role. Classical techniques such as sparse approximate inverse (SPAI) and wavelet-based preconditioners seek to transform (1) into

$$M^{-1}Ax = M^{-1}b, \quad (11)$$

where  $M \approx A^{-1}$  clusters the spectrum of  $M^{-1}A$  and suppresses low-energy modes that dominate convergence [32]. From a spectral viewpoint, these methods selectively mitigate the components responsible for large  $\kappa$ . This perspective closely parallels the motivation for the quantum subroutines considered in this work, which likewise aim to address the most problematic spectral components.

However, when implemented on fault-tolerant quantum hardware, preconditioning introduces additional circuit and space overheads. Modern QLSA achieve their favorable complexity by assuming efficient access to block-encodings or linear combination of unitaries (LCU) representations of  $A$ , implemented via SELECT and PREPARE oracles. While powerful, these constructions require ancillary registers whose size grows with the complexity of encoding the matrix coefficients. As demonstrated by explicit circuit realizations [33], the resulting ancilla overhead and control logic can dominate the overall space complexity, even when the oracle query complexity is asymptotically optimal.

In contrast, the original HHL algorithm operates directly through Hamiltonian simulation of  $A$  and does not require an explicit block-encoding or LCU representation. Although this leads to a less favorable asymptotic dependence on  $\kappa$ , it avoids the additional ancilla qubits needed to encode matrix coefficients. This reduced space overhead makes HHL particularly well suited for exploration in early fault-tolerant regimes, where logical qubits are scarce and architectural constraints are severe.

For these reasons, we focus on HHL rather than fully block-encoding-based QLSA in this work. Our goal is not to compete with the asymptotically optimal QLSA framework, but to assess the practical utility of quantum spectral techniques under realistic device constraints, and to understand how quantum and classical resources can be combined effectively within an integrated quantum-HPC platform.

### III. QUANTUM ACCELERATED CONJUGATE GRADIENT METHOD

In this section, we provide an integrated fault-tolerant quantum-HPC algorithm for LSP to address large-scale linear systems more efficiently than either resource alone under explicit spectral conditions. The strategy is based on the spectral decomposition of the coefficient matrix  $A$ . A quantum computer is employed to approximate the solution in a low-energy subspace via HHL, while CG is employed in the complementary subspace. We refer to this combined strategy as QACG. QACG is designed

as a cooperative integrated quantum-HPC system: the quantum subroutine performs a spectrally targeted initialization, while the classical CG solver carries out the main large-scale iterative refinement.

#### A. Warm-start conjugate gradients

We briefly explain CG by referring to the notation used in Ref. [26]. When  $A$  is SPD, CG can be interpreted as minimizing a quadratic function induced by the  $A$ -norm. Specifically, at iteration  $k$ , the approximation  $x_{(k)}$  minimizes

$$\|x - x_{(k)}\|_A^2 := (x - x_{(k)})^T A (x - x_{(k)}) \quad (12)$$

over the affine subspace determined by the previous iterates. Equivalently, CG minimizes the quadratic functional

$$f(x) := \frac{1}{2} x^T A x - b^T x, \quad (13)$$

whose first-order optimality condition is  $Ax = b$ . This variational characterization provides the basis for the recursive update rules of CG.

At each iteration, the next iterate is obtained by updating the current solution along a search direction  $p_{(k)}$ ,

$$x_{(k+1)} = x_{(k)} + \alpha_{(k)} p_{(k)}, \quad (14)$$

where the scalar  $\alpha_{(k)}$  is chosen to minimize the quadratic function along  $p_{(k)}$ . The search directions are constructed to be  $A$ -conjugate. Starting from the initial residual  $r_{(0)} = b - Ax_{(0)}$ , the first direction is set as  $p_{(0)} = r_{(0)}$ . Enforcing a Galerkin condition yields the coefficient

$$\alpha_{(k)} = \frac{(r_{(k)})^T r_{(k)}}{(p_{(k)})^T A p_{(k)}}. \quad (15)$$

The residuals evolve according to

$$r_{(k+1)} = r_{(k)} - \alpha_{(k)} A p_{(k)}, \quad (16)$$

and subsequent directions are generated by the standard two-term recurrence,

$$p_{(k+1)} = r_{(k+1)} + \frac{(r_{(k+1)})^T r_{(k+1)}}{(r_{(k)})^T r_{(k)}} p_{(k)}. \quad (17)$$

In particular, (16) shows that  $r_{(k+1)}$  is a linear combination of the previous residual  $r_{(k)}$  and the direction  $A p_{(k)}$ . When  $x_{(0)} \neq 0$ , the initial residual  $r_{(0)}$  encodes prior information about the solution, allowing CG to converge in fewer iterations depending on the quality of the warm start, up to effects caused by finite-precision arithmetic.

From the spectral convergence of iterative methods, the initial error can be decomposed into eigenmodes of

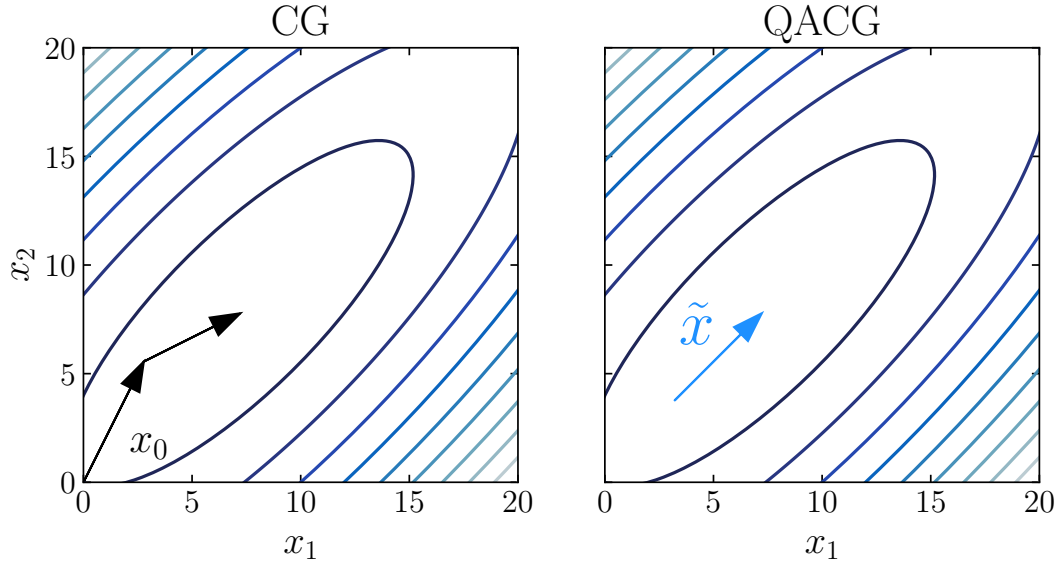


FIG. 1. Conceptual figure of the quantum-accelerated conjugate gradient (QACG) method. Left: CG starts a classical search with a zero vector  $x_{(0)}$  when there is no prior knowledge. Right: QACG first utilizes a quantum computer to generate an initial guess  $\tilde{x}$  in a low-energy subspace to accelerate the subsequent search by CG (blue arrow).

$A$ , and the components associated with small eigenvalues typically decay most slowly across iterations [34–38]. From another point of view, Ref. [39] provided a systematic mapping study of warm-start techniques in quantum computing and indicated potential advantage in quantum-to-classical warm-start algorithms. Having that said, suppressing these low-energy components in the initial error reduces the effective degrees of a polynomial required for convergence and can significantly reduce the number of CG iterations. The iterative structure of CG naturally exposes intermediate solution scales through the residuals  $\{r_{(k)}\}$ , which motivates the following problem formulation.

**Definition 1** (Quantum acceleration problem). *Let  $\hat{A}$  be an  $N \times N$  Hermitian matrix with known condition number  $\kappa$ ,  $\|\hat{A}\| = 1$ , and at most  $d$  nonzero entries in any row or column. Let  $|b\rangle$  be an  $N$ -dimensional vector encoded as a quantum state, and let  $x := A^{-1}b$ . We define*

$$|b\rangle := \frac{\sum_i b_i |i\rangle}{\|\sum_i b_i |i\rangle\|} \quad \text{and} \quad |\tilde{x}\rangle := \frac{\sum_i \tilde{x}_i |i\rangle}{\|\sum_i \tilde{x}_i |i\rangle\|}. \quad (18)$$

*The goal is to output a quantum state  $\tilde{\tilde{x}}$  such that  $\|\tilde{\tilde{x}}\rangle - |\tilde{x}\rangle\| \leq \varepsilon$ , succeeding with probability  $\Omega(1)$  with a flag indicating success.*

To have a vector  $|\tilde{x}\rangle$  that accelerates a conjugate gradient search, we consider incorporating modified HHL in the next section.

## B. Initial guess via the HHL algorithm

The original statement of quantum linear systems problem (QLSP) is defined as the task of preparing the quantum state [40]

$$|x\rangle = \hat{A}^{-1}|b\rangle, \quad (19)$$

where  $\hat{A}^{-1}$  denotes a normalized implementation of  $A^{-1}$  acting on the input state  $|b\rangle$ . With QACG, we approximate the inversion rather than reproducing the full inverse required for an end-to-end quantum linear solver, and we use the result only to warm-start CG. In particular, we apply a spectral filter that inverts only a low-energy window (below a cutoff  $\lambda_{\text{cutoff}}$ ), yielding an initialization that is sufficient to reduce the subsequent classical iteration count.

For the residual criterion  $r_{(k)} \leq \varepsilon$  that would otherwise require a Krylov space of order  $j$ , we truncate the inversion at order  $i$  by focusing on a low-energy subspace. For an initial residual  $r_{(0)} = b - Ax_{(0)}$ , the truncated Krylov subspace is denoted as

$$\mathcal{K}_i = \text{span} \{r_{(0)}, Ar_{(0)}, A^2r_{(0)}, \dots, A^{i-1}r_{(0)}\}. \quad (20)$$

With truncated Krylov subspaces  $\mathcal{K}_i$ , we define the fil-

tered inverse operator

$$\tilde{A}^{-1} = \sum_j \tilde{f}(\lambda_j) |\lambda_j\rangle\langle\lambda_j|, \quad (21)$$

$$\tilde{f}(\lambda, \lambda_{\text{cutoff}}) = \begin{cases} \frac{1}{\lambda}, & \lambda \leq \lambda_{\text{cutoff}}, \\ 0, & \lambda > \lambda_{\text{cutoff}}, \end{cases}$$

where  $\lambda_{\text{cutoff}}$  is an eigenvalue threshold defining the low-energy subspace. Applying  $\tilde{A}^{-1}$  produces the state

$$\begin{aligned} |\tilde{x}\rangle &= \tilde{A}^{-1}|b\rangle \\ &= \tilde{f}(\lambda)|\lambda\rangle\langle\lambda|b\rangle \\ &= c\tilde{f}(\lambda)|u\rangle, \end{aligned} \quad (22)$$

where  $c = \langle\lambda|b\rangle$  and  $|u\rangle$  denotes the normalized filtered component. Note that eigenvalue inversion with amplitude amplification can be improved to  $\mathcal{O}(\kappa \text{polylog}(\kappa))$  using Richardson extrapolation, whereas the straightforward implementation generally requires  $\mathcal{O}(\kappa^2)$  (see App. A for details).

The HHL algorithm [20] prepares this state through the composite unitary

$$\begin{aligned} \tilde{U}_{\text{HHL}}|0\rangle|0\rangle|0\rangle &= \left(\tilde{U}_{\text{QPE}}^\dagger C\tilde{R}_Y \tilde{U}_{\text{QPE}} \tilde{U}_{\text{INIT}}\right)|0\rangle|0\rangle|0\rangle \\ &= |0\rangle|u\rangle \left(\sqrt{1 - |c\tilde{f}(\lambda)|^2}|0\rangle + c\tilde{f}(\lambda)|1\rangle\right), \end{aligned} \quad (23)$$

where the ancilla state  $|1\rangle$  marks successful inversion with probability proportional to  $|c\tilde{f}(\lambda)|^2$ .

To amplify this component, one applies reflections in the amplitude amplification routine:

$$\tilde{U}_{\text{AA}}|0\rangle|0\rangle|0\rangle = (U_s \tilde{U}_\omega)^k \tilde{U}_{\text{HHL}}|0\rangle|0\rangle|0\rangle \quad (24)$$

$$\simeq \tilde{f}(\lambda)|0\rangle|u\rangle|1\rangle, \quad (25)$$

with

$$\begin{aligned} \tilde{U}_\omega &= \mathbb{I} - 2|\beta\rangle\langle\beta| := \tilde{U}_{\text{HHL}} U_0 \tilde{U}_{\text{HHL}}^\dagger, \\ U_s &= 2|s\rangle\langle s| - \mathbb{I} := 2(\mathbb{I} \otimes \mathbb{I} \otimes |1\rangle\langle 1|) - \mathbb{I}, \\ U_0 &= \mathbb{I} - 2|\mathbf{0}\rangle\langle\mathbf{0}|, \end{aligned} \quad (26)$$

which act as the oracle and diffusion operators.

**Algorithm 1** summarizes the complete procedure of QACG. The quantum condition number  $\kappa'$  is a parameter that determines the truncation order of subspaces to produce the quantum initial guess. Hence  $\kappa''$  plays an important role in the elapsed time to complete the whole procedure. We describe the optimization procedure in Sec. IV based on the COBYQA optimizer. Furthermore, we assume the `ClassicalDecode` function as an idealized interface that extracts task-relevant classical information from  $|\tilde{x}\rangle$  to warm-start CG.

---

**Algorithm 1:** Quantum-accelerated conjugate gradients (QACG)

---

**Input:** Hermitian matrix  $A \in \mathbb{C}^{n \times n}$ , right-hand side  $b \in \mathbb{C}^n$ , tolerance  $\varepsilon$ , quantum condition number  $\kappa'$   
**Output:** Approximate solution  $x_{(k)}$  to  $Ax = b$   
 Perform HHL with effective condition number  $\kappa'$ , prepare a quantum state proportional to  $\tilde{A}^{-1}|b\rangle$ , and use it to initialize the classical iterate:

$$|\tilde{x}\rangle = \frac{\tilde{A}^{-1}|b\rangle}{\|\tilde{A}^{-1}|b\rangle\|}, \quad x_{(0)} = \text{ClassicalDecode}(|\tilde{x}\rangle).$$

$$r_{(0)} = b - Ax_{(0)}$$

$$p_{(0)} = r_{(0)}$$

$$k = 0$$

**while** not close enough to solution **do**

$$\alpha_{(k)} = \frac{(r_{(k)})^T r_{(k)}}{(p_{(k)})^T A p_{(k)}}$$

$$x_{(k+1)} = x_{(k)} + \alpha_{(k)} p_{(k)}$$

$$r_{(k+1)} = r_{(k)} - \alpha_{(k)} A p_{(k)}$$

$$p_{(k+1)} = r_{(k+1)} + \frac{(r_{(k+1)})^T r_{(k+1)}}{(r_{(k)})^T r_{(k)}} p_{(k)}$$

$$k = k + 1$$

**end**

---

We emphasize that QACG does not rely on an exact classical readout (full state tomography) of  $|\tilde{x}\rangle$ . Instead, it suffices to obtain a classical approximation that is accurate enough for warm-starting CG, i.e., within a controlled approximation error that leads to a reduced initial residual.

Instead of assuming an exact classical readout of the quantum state  $|\tilde{x}\rangle$ , we assume that task-relevant classical information sufficient for warm-starting CG can be obtained via classical approximation of the quantum state. In particular, structured quantum states such as  $|\tilde{x}\rangle$  may admit efficient classical approximations with polynomial computational cost and controllable approximation error, for example by using tensor network representations [41] or via polynomial expansions [42–44]. Such approximations need only preserve the components relevant to reducing the initial residual of CG, rather than reproducing the full quantum state exactly.

### C. Quantum circuit for the 3D Poisson equation

A fundamental example of LSP is an elliptic PDE such as the Poisson equation. Here, we define explicit quantum circuits of QACG for the 3D Poisson equation to enable a concrete discussion of time complexity in Sec. IV. We define the Poisson equation as follows.

**Definition 2** (Finite difference Poisson equation). *Let  $\Omega = (0, 1)^3$  be the unit cube. Consider the 3D Poisson*

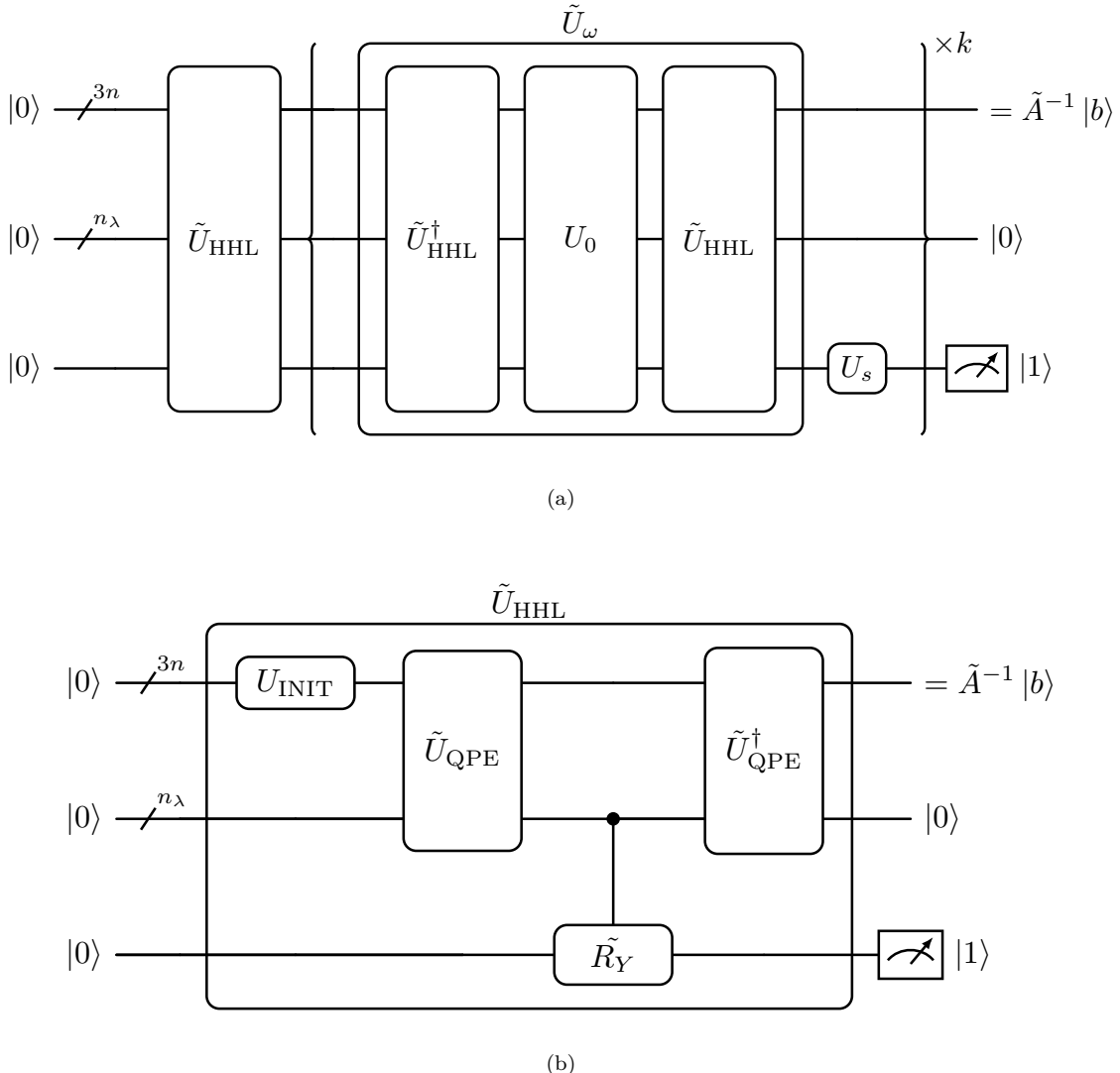


FIG. 2. Quantum circuits used to construct an initial guess for the 3D Poisson equation: (a) amplitude amplification applied to boost the success probability of the solution state and (b) the HHL operator composed of state preparation, quantum phase estimation, and controlled rotation to implement a spectrally filtered matrix inversion.

equation with periodic boundary conditions

$$\begin{aligned} -\Delta u(\mathbf{x}) &= f(\mathbf{x}) & \text{for } \mathbf{x} \in \Omega, \\ u(\mathbf{x}) &= 0 & \text{for } \mathbf{x} \in \partial\Omega. \end{aligned} \quad (27)$$

Discretize (27) by second-order finite differences on a uniform cell-centered grid with spacing  $h = 1/n$  and  $n$  points per coordinate direction, so that the total number

of unknowns is  $N = n^3$ . Denote grid points by

$$\begin{aligned} x_i &= \left(i - \frac{1}{2}\right) h, & i &= 1, \dots, n, \\ y_j &= \left(j - \frac{1}{2}\right) h, & j &= 1, \dots, n, \\ z_k &= \left(k - \frac{1}{2}\right) h, & k &= 1, \dots, n, \end{aligned} \quad (28)$$

and write  $x_{i,j,k} \approx u(x_i, y_j, z_k)$ ,  $f_{i,j,k} \approx f(x_i, y_j, z_k)$ . The standard 7-point stencil yields, for interior indices  $(i, j, k)$  with ghost-cell eliminations encoding  $u = 0$  on  $\partial\Omega$ . Vectorizing the unknowns, the scheme induces a sparse SPD matrix  $A \in \mathbb{R}^{N \times N}$  with 7 non-zero entries per row (up to boundaries) such that  $Ax = b$  matches (1).

To compute an initial guess  $|\tilde{x}\rangle$ , one must design and implement quantum circuits for a given  $A$  and  $b$ . In this work, we consider implementing HHL along with amplitude amplification as displayed in [FIG. 2](#). The operator  $\tilde{U}_{\text{HHL}}$  (and  $\tilde{U}_{\text{HHL}}^\dagger$ ) is composed of state preparation  $\tilde{U}_{\text{INIT}}$ , QPE blocks  $\tilde{U}_{\text{QPE}}$ ,  $\tilde{U}_{\text{QPE}}^\dagger$ , and controlled rotation  $\tilde{R}_Y$ . The circuit  $\tilde{U}_{\text{INIT}}$  prepares  $|b\rangle$ , QPE estimates eigenvalues of  $A$ , and the controlled rotation  $\tilde{R}_Y$  inverts the spectrum to implement the filtered matrix inversion.

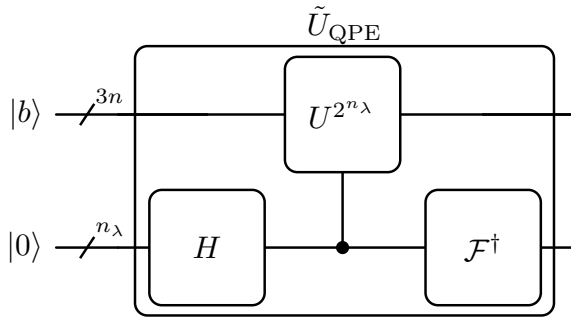


[FIG. 3](#). Quantum phase estimation circuit used within HHL to coherently encode eigenvalue information of the system matrix. Controlled time-evolution unitaries and an inverse quantum Fourier transform map eigenphases onto a phase register, enabling subsequent controlled rotations that implement spectral inversion.

To estimate the eigenvalues of the system matrix and enable spectral inversion, we implement QPE as a core subroutine within the HHL framework. As shown in [FIG. 3](#), the QPE block  $\tilde{U}_{\text{QPE}}$  consists of an  $n_\lambda$ -qubit phase register initialized in  $|0\rangle$ , followed by a layer of Hadamard gates to create a uniform superposition. Controlled applications of the unitary powers  $U^{2^{n_\lambda}}$  encode the eigenphases via phase kickback, where  $U = \exp(iAt)$  is the time-evolution operator associated with the system matrix  $A$ .

For the specific case of the 3D Poisson equation considered here, the implementation of the controlled powers  $U^{2^{n_\lambda}}$  can be substantially abbreviated relative to a generic sparse Hamiltonian. The discretized Laplacian matrix is diagonalizable, implying that its eigenvalues are available in closed form and that the corresponding time-evolution operator can be synthesized without explicitly constructing  $2^{n_\lambda}$  sequential applications of  $U$ . Instead, the controlled  $U^{2^{n_\lambda}}$  operations can be realized by reusing a common circuit structure with appropriately rescaled evolution times. As a result, the cost of implementing  $U^{2^{n_\lambda}}$  scales with the precision of the phase estimation rather than exponentially with  $n_\lambda$ .

An inverse quantum Fourier transform  $\mathcal{F}^\dagger$  is then applied to the phase register to obtain a binary approximation of the eigenvalues  $\lambda_j$  of  $A$ , coherently correlated with the corresponding eigenstates in the data register. This eigenvalue information is subsequently used in the

controlled rotation  $\tilde{R}_Y$  to implement spectral inversion, completing the HHL procedure.

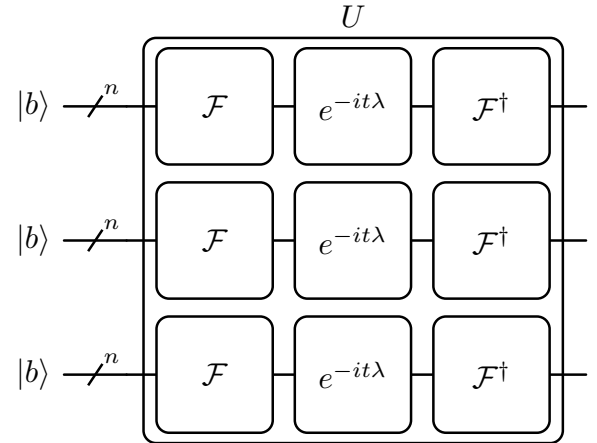


[FIG. 4](#). Quantum circuit implementing the unitary  $U = \exp(iAt)$  for the 3D periodic Laplacian via spectral decomposition. By applying quantum Fourier transforms on each spatial register, performing diagonal phase rotations corresponding to the Laplacian eigenvalues, and uncomputing the Fourier basis, the circuit realizes exact time evolution under the separable 3D Laplacian.

For periodic boundary conditions, the Laplacian is diagonal in the Fourier basis. In the continuous setting, with Fourier transform  $\hat{u}(\kappa) = \mathcal{F}[u](\kappa)$ , one has

$$\mathcal{F}[\Delta u](\kappa) = -\|\kappa\|_2^2 \hat{u}(\kappa), \quad \kappa = (\kappa_x, \kappa_y, \kappa_z). \quad (29)$$

Thus,  $\Delta$  is diagonalized by  $\mathcal{F}$  with eigenvalue  $-\|\kappa\|_2^2$ .

In the discrete periodic case, the 1D circulant Laplacian  $A$  in [Definition 5](#) is diagonalized by the discrete Fourier transform (DFT) matrix  $F$ :

$$A = F^\dagger \Lambda F, \quad \Lambda = \text{diag}(\lambda_0, \dots, \lambda_{n-1}), \quad (30)$$

with eigenvalues (for mode index  $k \in \{0, \dots, n-1\}$ )

$$\lambda_k = \frac{4}{h^2} \sin^2 \left( \frac{\pi k}{n} \right). \quad (31)$$

The 3D discrete Laplacian on an  $n \times n \times n$  periodic grid is separable and can be written as a Kronecker sum

$$A = A \otimes I \otimes I + I \otimes A \otimes I + I \otimes I \otimes A, \quad (32)$$

so it is diagonalized as

$$A = F^\dagger \Lambda F, \quad \Lambda = \text{diag}(\lambda_{k_x, k_y, k_z}), \quad (33)$$

where the eigenvalue associated with the Fourier mode  $(k_x, k_y, k_z)$  is the additive combination

$$\lambda_{k_x, k_y, k_z} = \lambda_{k_x} + \lambda_{k_y} + \lambda_{k_z}. \quad (34)$$

Consequently, the unitary  $U = \exp(iAt)$  admits the spectral implementation [45, 46]

$$U = \mathcal{F}^\dagger \exp(it\Lambda) \mathcal{F}, \quad (35)$$

which matches the circuit in [FIG. 4](#): apply  $\mathcal{F}^{\otimes 3}$  (a QFT on each spatial register) to move to the Fourier basis, apply a diagonal phase rotation that maps  $|k_x, k_y, k_z\rangle \mapsto e^{it\lambda_{k_x, k_y, k_z}}|k_x, k_y, k_z\rangle$ , and finally apply  $(\mathcal{F}^\dagger)^{\otimes 3}$  to return to the computational basis.

The right-hand side vector  $|b\rangle$  must be efficiently encoded into a quantum state in order to apply HHL. In this work, we employ the Fourier-series loader (FSL) introduced in [\[47\]](#), which provides a scalable and structured approach to quantum state preparation based on truncated Fourier expansions and uniformly controlled rotations.

Let  $b(x)$  be a real-valued function defined on a uniform grid of size  $n$ , corresponding to the discretized right-hand side vector

$$|b\rangle = \frac{1}{\|b\|} \sum_{x=0}^{n-1} b(x)|x\rangle. \quad (36)$$

The FSL approach approximates  $b(x)$  by a truncated Fourier series

$$b(x) \approx \sum_{k=-m}^m c_k e^{2\pi i k x / n}, \quad (37)$$

where  $c_k$  are Fourier coefficients and  $m \ll n$  controls the truncation error. For sufficiently smooth functions  $b(x)$ , the approximation error decays exponentially in  $m$ , making the method suitable for vectors arising from PDE discretizations.

The corresponding quantum circuit is shown in [FIG. 5](#). The circuit first prepares an intermediate state on an  $(m+1)$ -qubit register in each direction using a cascaded entangler  $U_c$ , which maps

$$|0\rangle^{\otimes(m+1)} \mapsto |c\rangle, \quad (38)$$

where

$$|c\rangle = 2^{-n/2} \sum_{k=0}^m c_k |k\rangle + 2^{-n/2} \sum_{k=1}^m c_{-k} |2^{m+1} - k\rangle. \quad (39)$$

This state coherently encodes both positive- and negative-frequency Fourier coefficients in a compact binary representation.

Next, a cascade of  $n-m-1$  CNOT gates entangles the coefficient register with the remaining qubits, mapping

$$|0\rangle^{\otimes(n-m-1)} \otimes |c\rangle \mapsto |c'\rangle, \quad (40)$$

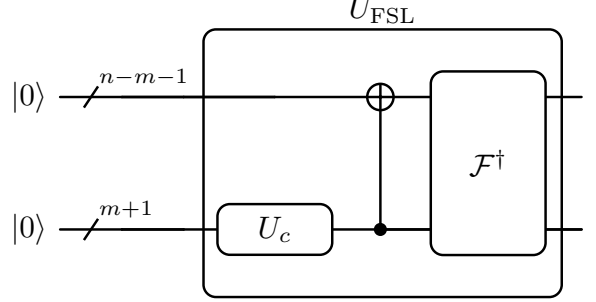


[FIG. 5](#). Quantum circuit for the 1D Fourier-series loader (FSL). The cascaded entangler  $U_c$  prepares a truncated Fourier-coefficient state on an  $(m+1)$ -qubit register, which is then entangled with the remaining qubits via CNOT ladders and mapped to the spatial domain by an inverse QFT, yielding  $|\tilde{b}\rangle$ .

where the resulting  $n$ -qubit state is

$$|c'\rangle = 2^{-n/2} \sum_{k=0}^m c_k |k\rangle + 2^{-n/2} \sum_{k=1}^m c_{-k} |2^n - k\rangle. \quad (41)$$

This step distributes the truncated Fourier coefficients across the full computational register.

Finally, an inverse quantum Fourier transform  $\mathcal{F}^\dagger$  is applied, yielding

$$\mathcal{F}^\dagger |c'\rangle \approx |b\rangle, \quad (42)$$

where the approximation error is controlled solely by the truncation order  $m$  in 1D.

The circuit depth of the FSL scales as  $\mathcal{O}(\log n + 2^m)$  assuming the Fourier coefficients  $c_k$  are classically pre-computed. Since  $m$  is fixed independently of  $n$  in our setting, this construction is compatible with large-scale quantum-HPC regimes. Moreover, both the FSL and HHL operate naturally in the spectral domain, so the prepared state integrates directly with the eigenvalue filtering  $\tilde{f}(\lambda)$  applied during QPE. As a result, the FSL-prepared vector emphasizes low-frequency components of  $|b\rangle$ , yielding an initial guess that captures the low-energy structure of the Krylov subspace associated with the discretized Laplacian.

Integrating the above procedures yields an initial guess  $x_{(0)}$  aligned with the spectral initialization. In the next subsection, we estimate the time complexity of CG, HHL, and QACG.

#### IV. TIME COMPLEXITY

In this section, we derive time-complexity models for solving the 3D Poisson equation ([Definition 2](#)) using CG, HHL, and QACG, assuming a partially fault-tolerant im-

plementation on a STAR-architecture quantum device.

### A. Conjugate gradient method

We begin by estimating the iteration complexity of CG to estimate the runtime on HPC.

**Lemma 1** (Iteration complexity of CG). *Consider the Poisson problem in [Definition 2](#) with the sparsity of [Lemma 4](#) and the condition number of [Lemma 3](#). Then, to guarantee a relative  $A$ -norm reduction*

$$\|x - x^{(k)}\|_A \leq \varepsilon \|x - x^{(0)}\|_A, \quad (43)$$

it suffices to perform at most

$$\mathcal{F}_{CG}(\kappa, \varepsilon) \geq \frac{1}{2} \sqrt{\kappa} \ln \left( \frac{2}{\varepsilon} \right) \quad (44)$$

iterations.

*Proof.* A standard CG convergence bound [26] gives

$$\frac{\|x - x^{(k)}\|_A}{\|x - x^{(0)}\|_A} \leq 2 \left( \frac{\sqrt{\kappa} - 1}{\sqrt{\kappa} + 1} \right)^k. \quad (45)$$

Solving  $2 \left( \frac{\sqrt{\kappa} - 1}{\sqrt{\kappa} + 1} \right)^k \leq \varepsilon$  yields

$$k \leq \left\lceil \frac{1}{2} \sqrt{\kappa} \ln \left( \frac{2}{\varepsilon} \right) \right\rceil, \quad (46)$$

which proves the claim.  $\square$

We estimate the number of floating-point operations required per CG iteration as follows. The analysis assumes a sparse matrix representation and a conventional implementation of the algorithm as given in [Algorithm 1](#). A dot product of two vectors of length  $n$  requires  $n$  multiplications and  $n - 1$  additions and therefore costs  $2n - 1$  floating-point operations. A scaled vector addition of the form  $y = y + \alpha x$  requires  $n$  multiplications and  $n$  additions and therefore costs  $2n$  floating-point operations. A sparse matrix-vector product  $w = Av$ , where  $A$  has  $\text{nnz}(A)$  nonzero entries, requires approximately  $2 \text{nnz}(A)$  floating-point operations, corresponding to one multiplication and one addition per nonzero. Scalar operations, such as divisions and assignments, contribute only a constant number of floating-point operations per iteration and are negligible for large  $n$ .

During each CG iteration, a single sparse matrix-vector product  $Ap_{(k)}$  is computed. This operation dominates the iteration cost and contributes approximately  $2 \text{nnz}(A)$  floating-point operations, with  $\text{nnz}(A)$  given by [Lemma 4](#). In addition, inner products are required to compute the step size and the conjugacy coefficient. Specifically, the quantities  $\{r_{(k)}^T r_{(k)}, p_{(k)}^T Ap_{(k)}, r_{(k+1)}^T r_{(k+1)}\}$  are evaluated, each

costing  $2n - 1$  floating-point operations. The update of the solution vector and the residual vector requires two scaled vector additions, contributing  $4n$  floating-point operations. The update of the search direction involves one additional scaled vector addition, contributing  $2n$  floating-point operations. Collecting these contributions yields the per-iteration operation count

$$\begin{aligned} F_{HPCG}(n) &\approx 2\text{nnz}(A) + 3(2n - 1) + 6n \\ &\approx 2\text{nnz}(A) + 12n. \end{aligned} \quad (47)$$

To translate this count into elapsed time, we calibrate it using the HPCG benchmark [48] on a specific HPC platform with the following model.

**Definition 3** (HPC model). *Let an HPC platform deliver a sustained floating-point throughput of  $T$  [flop/s] for a given workload class. Let  $F$  denote the total number of floating-point operations (flops) executed by an algorithm. We define the expected wall-clock time as*

$$\mathcal{T}(F, T) = \frac{F}{T}. \quad (48)$$

Equivalently, if an algorithm consists of  $N$  iterations, each costing  $F_{\text{iter}}$  flops, then

$$\mathcal{T} = \frac{NF_{\text{iter}}}{T}. \quad (49)$$

With the above model, we state the time complexity of CG on an HPC platform as follows.

**Theorem 1** (Time complexity of HPCG). *Consider solving the Poisson linear system using CG on an HPC platform characterized by [Definition 3](#). Let  $F_{HPCG}(n)$  denote the floating-point operation count per CG iteration for problem size parameter  $n$ , and let  $\mathcal{F}_{CG}(\kappa, \varepsilon)$  be the iteration complexity from [Lemma 1](#). Then the expected wall-clock time satisfies*

$$\mathcal{T}_{HPCG}(T, n, \kappa, \varepsilon) = \frac{F_{HPCG}(n)}{T} \mathcal{F}_{CG}(\kappa, \varepsilon). \quad (50)$$

*Proof.* From [Lemma 1](#), CG requires

$$N = \mathcal{F}_{CG}(\kappa, \varepsilon) \quad (51)$$

iterations to reach accuracy  $\varepsilon$ , where  $\kappa$  is the relevant condition number.

Each iteration executes

$$F_{\text{iter}} = F_{HPCG}(n) \quad (52)$$

floating-point operations. Therefore, the total operation count is

$$F = NF_{\text{iter}} = \mathcal{F}_{CG}(\kappa, \varepsilon) F_{HPCG}(n). \quad (53)$$

Applying [Definition 3](#) yields

$$\mathcal{T}_{\text{HPCG}}(T, n, \kappa, \varepsilon) = \frac{F}{T} = \frac{F_{\text{HPCG}}(n)}{T} \mathcal{F}_{\text{CG}}(\kappa, \varepsilon), \quad (54)$$

which proves the claim.  $\square$

To account for the fact that the HPC platform is shared among multiple users and that a single job does not occupy the full machine continuously, we introduce an effective utilization delay modeled as a multiplicative factor of  $10^{-2}$  applied to floating-point throughput. Concretely, we assume that only one percent of the nominal sustained floating-point performance is available to the job on average. This  $10^{-2}$  delay is intended as an effective model of distributed platform usage, including job scheduling, queueing, and resource sharing, rather than as a hardware-level slowdown.

In particular, we consider the SoftBank Corp. CHIE-4 platform. The HPCG benchmark ([TOP500.org, https://top500.org/lists/hpcg/2025/11/](https://top500.org/lists/hpcg/2025/11/); accessed 10 February 2026) reports  $3.76 \times 10^{15}$  floating-point operations per second, indicating a sustained throughput of  $T_{\text{CHIE-4}} \approx 3.76 \text{ PFlop/s}$  on this workload. The HPCG benchmark accounts for overheads by using a realistic solver that includes a three-level multigrid preconditioner (with Gauss–Seidel smoothing) and frequent global reductions, thus providing a representative performance measure beyond idealized peak throughput. Incorporating the  $10^{-2}$  utilization factor, we define an effective throughput

$$T_{\text{CHIE-4}}^{\text{eff}} = 10^{-2} T_{\text{CHIE-4}}, \quad (55)$$

which we use for wall-clock time estimates.

Substituting [Lemma 1](#) into [Theorem 1](#) then yields

$$\begin{aligned} \mathcal{T}_{\text{CHIE-4}}(n, \kappa, \varepsilon) &= \frac{F_{\text{HPCG}}(n)}{T_{\text{CHIE-4}}^{\text{eff}}} \mathcal{F}_{\text{CG}}(\kappa, \varepsilon) \\ &\approx \frac{F_{\text{HPCG}}(n)}{T_{\text{CHIE-4}}^{\text{eff}}} \cdot \frac{1}{2} \sqrt{\kappa} \ln \left( \frac{2}{\varepsilon} \right). \end{aligned} \quad (56)$$

This expression estimates  $\mathcal{T}_{\text{CHIE-4}}$  in seconds for given  $n, \kappa, \varepsilon$  under shared-platform operation. Please note that the HPCG benchmark [48] evaluates  $\text{nnz}(A)$  using a different coefficient matrix  $A$ ; therefore, an effective  $\text{nnz}(A)$  must be substituted into  $F_{\text{HPCG}}(n)$  to obtain a correct calibration for the problem instance considered here.

Finally we emphasize that the above runtime model should be interpreted as a conservative upper bound. While the theoretical iteration count scales as  $\mathcal{O}(\sqrt{\kappa})$  for unpreconditioned CG, the HPCG benchmark employs a multigrid-preconditioned solver that often converges in a nearly constant number of iterations in practice for Poisson-type problems. In this work, we retain the  $\mathcal{O}(\sqrt{\kappa})$  dependence as a worst-case estimate to enable a uniform, hardware-calibrated comparison across different algorithms.

## B. HHL algorithm

We state the partially fault-tolerant quantum device model to consider in the rest of the work.

**Definition 4** (STAR architecture model). *We define a gate set*

$$\mathcal{U} = \{\mathcal{U}_{\text{Clifford}}, R_Z\}, \quad \mathcal{U}_{\text{Clifford}} = \{H, S, \text{CNOT}\}, \quad (57)$$

and introduce the architecture constants

$$\mathcal{P} = \{d, \tau, r\}, \quad (58)$$

with

$$\begin{aligned} d \in \mathbb{Z}_{\geq 1} &\quad (\text{code distance}), \\ \tau > 0 &\quad (\text{QEC cycle time}), \\ r \in \mathbb{Z}_{\geq 1} &\quad (\text{RUS steps}), \end{aligned} \quad (59)$$

with RUS stands for repeat-until-success. For the gates

$$U \in \mathcal{U}, \quad U_{\text{Clifford}} \in \mathcal{U}_{\text{Clifford}}, \quad (60)$$

we define the expected gate time by

$$\mathcal{T}(U) \in \mathbb{R}_{\geq 0} \quad (61)$$

as follows:

$$\begin{aligned} \mathcal{T}(H) &= 3d\tau, \\ \mathcal{T}(S) &= 2d\tau, \\ \mathcal{T}(\text{CNOT}) &= 2d\tau, \\ \mathcal{T}(R_Z) &= 2r\tau. \end{aligned} \quad (62)$$

The STAR architecture model adopted here is consistent with recent proposals for quantifying fault-tolerant quantum performance using quantum logical operations per second (QLOPS) [49]. In that framework, the effective throughput is modeled as

$$Q = k \times \frac{1}{(\lceil t_r/t_{\text{SEC}} \rceil + d)t_{\text{SEC}}}, \quad (63)$$

where  $t_{\text{SEC}}$  denotes the syndrome extraction cycle time,  $d$  is the code distance,  $t_r$  is the classical reaction time, and  $k$  captures architectural parallelism. This expression highlights that, at the logical level, performance is primarily governed by the cadence of QEC cycles and the code distance, while classical reaction latency enters only as an additive overhead in units of  $t_{\text{SEC}}$ .

Motivated by this observation, the STAR model abstracts each logical gate as an independent operation with an expected duration proportional to  $d\tau$ , where  $\tau$  plays the role of the QEC cycle time. We do not explicitly model the reaction time  $t_r$  or pipeline effects; instead, these contributions are implicitly absorbed into constant prefactors in the expected gate times. This abstraction is appropriate for the present analysis, which

focuses on asymptotic scaling and relative resource trade-offs rather than absolute peak throughput. By treating logical gates individually and accounting for repeat-until-success (RUS) overheads at the gate level, the STAR model captures the dominant dependence on QEC cadence and code distance identified by the QLOPS metric, while remaining sufficiently simple to support transparent algorithm-level resource estimation under partial fault tolerance.

**Theorem 2** (Time complexity of HHL). *Consider the HHL with amplitude amplification to solve LSP with Definition 2 that is parameterized by  $n$ , the unknowns in 1D,  $\kappa$ , the condition number, and  $\varepsilon$ , the tolerance. Moreover, consider a partially fault-tolerant quantum computer whose universal gate set and the execution time are defined by Definition 4. Then the expected runtime is given by*

$$\begin{aligned} & \mathcal{T}_{HHL}(d, \tau, r, n, \kappa, \varepsilon) \\ &= 3d\tau\mathcal{G}_H(\log n, \kappa, \varepsilon) \\ &+ 2d\tau[\mathcal{G}_S(\log n, \kappa, \varepsilon) + \mathcal{G}_{CNOT}(\log n, \kappa, \varepsilon)] \\ &+ 2rd\tau\mathcal{G}_{R_Z}(\log n, \kappa, \varepsilon). \end{aligned} \quad (64)$$

with  $d$  here the code distance,  $\tau$  the QEC cycle time,  $r$  the RUS steps.

*Proof.* The expected time of each gate follows from Definition 4; summing over the gate counts yields the stated expression. The concrete derivation of gate counts is provided by Definition 8 in App. B.  $\square$

### C. Quantum-accelerated conjugate gradient method

We now estimate the runtime of QACG. We distinguish two effective condition numbers in QACG. Let  $\kappa$  be the spectral condition number of  $A$  on the full space. The quantum initialization uses a spectrally filtered inverse  $\tilde{A}^{-1}$  (Sec. III), which effectively restricts inversion to a low-energy spectral window; we denote by  $\kappa'$  the resulting effective condition number that determines the cost of the HHL-based preparation of  $|\tilde{x}\rangle$ . After initializing the iterate with the decoded vector  $x_{(0)}$ , the subsequent HPCG stage solves the remaining residual problem, whose convergence is governed by an effective condition number  $\kappa''$  that depends on the quality of the warm start. Thus,  $\kappa'$  parameterizes the quantum cost, while  $\kappa''$  parameterizes the classical refinement cost.

**Theorem 3** (Time complexity of QACG). *Consider QACG to solve LSP with Definition 2 that is parameterized by  $n$ , the unknowns in 1D,  $\kappa$ , the condition number, and  $\varepsilon$ , the tolerance. Moreover, consider a HPC model in Definition 3, equipped with a partially fault-tolerant quantum computer whose universal gate set and the execution time are defined by Definition 4. Let the algorithm consist of (i) a spectral initialization stage implemented*

by HHL, followed by (ii) a classical CG stage. Then, combining Theorem 1 and Theorem 2, the expected total runtime satisfies

$$\begin{aligned} & \mathcal{T}_{QACG}(T, d, \tau, r, n, \kappa', \kappa'', \varepsilon) \\ &= \mathcal{T}_{HHL}(d, \tau, r, n, \kappa', \varepsilon) + \mathcal{T}_{HPCG}(T, n, \kappa'', \varepsilon), \end{aligned} \quad (65)$$

where  $\kappa'$  is the quantum condition number used in the spectral initialization (e.g.,  $\kappa' = \lambda_{\text{cutoff}}/\lambda_{\text{min}}$ ), and  $\kappa''$  is the effective condition number governing the residual system solved by the subsequent classical CG stage. In addition, we denote  $T$  [flop/s] the sustained floating-point throughput for HPC,  $d$  the code distance of a quantum device,  $\tau$  the QEC cycle time,  $r$  the RUS steps.

*Proof.* We analyze QACG as a two-stage procedure applied to the QAP instance (Definition 1), where the initial iterate  $x_{(0)}$  is produced by spectral initialization (22) and then refined by HPCG.

By Theorem 2, preparing  $|\tilde{x}\rangle$  with quantum condition number  $\kappa' := \lambda_{\text{cutoff}}/\lambda_{\text{min}}$  has expected runtime

$$\mathcal{T}_{HHL}(d, \tau, r, n, \kappa', \varepsilon). \quad (66)$$

Write the spectral decomposition of the right-hand side in the eigenbasis  $\{|\lambda_j\rangle\}_j$  of  $A$ :

$$|b\rangle = \sum_j b_j |\lambda_j\rangle, \quad b_j := \langle \lambda_j | b \rangle. \quad (67)$$

The spectral initialization produces a filtered state

$$|\tilde{x}\rangle = \sum_j \tilde{f}(\lambda_j) b_j |\lambda_j\rangle, \quad (68)$$

where  $\tilde{f}(\cdot)$  approximates  $1/\lambda$  on the spectral region retained by the cutoff.

Let the classical initial iterate be obtained by a decoding map  $x_{(0)} = \text{ClassicalDecode}(|\tilde{x}\rangle)$  as discussed in Sec. III. Consider the action of  $A$  on the initializer:

$$\begin{aligned} A|\tilde{x}\rangle &= A \sum_j \tilde{f}(\lambda_j) b_j |\lambda_j\rangle \\ &= \sum_j \lambda_j \tilde{f}(\lambda_j) b_j |\lambda_j\rangle. \end{aligned} \quad (69)$$

Hence the residual associated with the initializer is

$$\begin{aligned} r_{(0)} &= b - Ax_{(0)} \\ &= \sum_j (1 - \lambda_j \tilde{f}(\lambda_j)) b_j |\lambda_j\rangle \\ &= \sum_j \alpha_j |\lambda_j\rangle, \end{aligned} \quad (70)$$

where

$$\alpha_j := (1 - \lambda_j \tilde{f}(\lambda_j)) b_j. \quad (71)$$

The subsequent CG refinement operates on the Krylov subspace generated by this residual,

$$\mathcal{K}_m = \text{span}\{r_{(0)}, Ar_{(0)}, A^2r_{(0)}, \dots, A^{m-1}r_{(0)}\}, \quad (72)$$

and its convergence rate is governed by an effective condition number  $\kappa''$  determined by the spectrum of  $A$  restricted to the support of  $r_{(0)}$ .

By [Theorem 1](#), the expected runtime of the classical refinement on the HPC model ([Definition 3](#)) is

$$\mathcal{T}_{\text{HPCG}}(T, n, \kappa'', \varepsilon). \quad (73)$$

The two stages are executed sequentially, so the expected total runtime is the sum

$$\begin{aligned} \mathcal{T}_{\text{QACG}}(T, d, \tau, r, n, \kappa', \kappa'', \varepsilon) \\ = \mathcal{T}_{\text{HHL}}(d, \tau, r, n, \kappa', \varepsilon) + \mathcal{T}_{\text{HPCG}}(T, n, \kappa'', \varepsilon), \end{aligned} \quad (74)$$

which proves the claim.  $\square$

## V. RESULT

In this section, we present estimated runtimes and resource requirements obtained by applying the time-complexity results derived in [Theorem 1](#), [Theorem 2](#), and [Theorem 3](#). For CG, the runtime is estimated using publicly available results from the HPCG benchmark on the SoftBank Corp. HPC platform CHIE-4, as discussed in [Sec. IV](#). For HHL and QACG, we evaluate fault-tolerant quantum costs at the logical level with [Definition 4](#). Specifically, we assume an QEC cycle time  $\tau \in \{1 \mu\text{s}, 1 \text{ ns}\}$  to examine both conservative near-term and optimistic future hardware scenarios. The code distance and the RUS steps are fixed at  $d = 7$  and  $r = 2$ , which we assume are sufficient to suppress logical errors to a level compatible with the target circuit depth considered in this work. Further more, we set the truncation order  $m = 10$  for FSL and  $p = 1$  for the parallel polynomial evaluation (see [App. B](#) for the detail). All quantum gate counts are converted into time estimates using [Definition 4](#).

A distinctive feature of QACG is that effective conditioning is decomposed into two parts, parameterized by a cutoff  $\lambda_{\text{cutoff}}$ : the quantum stage targets the low-energy window  $[\lambda_{\text{min}}, \lambda_{\text{cutoff}}]$ , and the classical stage refines the remaining spectral content in  $[\lambda_{\text{cutoff}}, \lambda_{\text{max}}]$ . We denote the corresponding effective condition numbers by  $\kappa'$  and  $\kappa''$ , respectively. By tuning this decomposition, one controls the quality of the initial solution provided by the quantum subroutine and thereby balances the computational burden between quantum and classical resources. Within this model, the allocation of the conditioning between  $\kappa'$  and  $\kappa''$  is determined by minimizing the total runtime using the COBYQA (version 1.1.3; <https://www.cobyqa.com>; accessed 4 February 2026). We set the tolerance for CG, HHL, and QACG equally as  $\varepsilon = 10^{-6}$ . In the rest of the work, we restrict

attention to a serial execution model in which quantum and classical computations are performed sequentially rather than in parallel.

### A. Runtime estimation

[FIG. 6](#) summarizes the expected runtime of the proposed QACG, compared against classical CG executed on an HPC system and full HHL. The left panel of [FIG. 6](#) shows the expected runtime as a function of problem size  $n$  for two representative QEC cycle times,  $\tau = 1 \mu\text{s}$  and  $\tau = 1 \text{ ns}$ . In the conservative setting  $\tau = 1 \mu\text{s}$ , the runtime of full HHL grows rapidly with  $n$ , reflecting its dependence on the full condition number  $\kappa$ . QACG substantially reduces this growth by optimizing the effective quantum condition number  $\kappa'$ , almost at the crossover scale  $n \approx 2^{12}$ , while classical CG on HPC remains faster than QACG.

In contrast, when the QEC cycle time is reduced to  $\tau = 1 \text{ ns}$ , the balance shifts qualitatively. In this regime, QACG achieves a lower expected runtime than classical CG starting at approximately  $n \approx 2^{12}$ , and the separation between the two methods widens with increasing  $n$ . These trends highlight the critical role of the QEC cycle time in enabling runtime advantages: only when the quantum subroutine can be executed sufficiently fast does the redistribution of conditioning between quantum and classical resources translate into a net speedup.

The right panel of [FIG. 6](#) shows the eigenvalue spectrum  $\{\lambda_j\}$  of the Poisson operator, together with the spectral initialization windows employed by QACG at  $n = 2^{12}$ . The vertical dashed lines indicate the index  $j$  up to which the low-energy subspace is handled by the quantum subroutine. For  $\tau = 1 \mu\text{s}$ , the optimal window corresponds to  $j = 2$ , which lies to the spectral origin under periodic boundary conditions. In this case, the quantum initialization covers only a negligible portion of the spectrum, explaining why QACG does not outperform classical CG in the left panel. By contrast, for  $\tau = 1 \text{ ns}$ , the optimal window expands to  $j = 12$ , indicating that a substantially larger low-energy subspace can be handled on a quantum computer. The fast generation of an initial guess in this low-energy sector enables a more effective reduction of the classical iteration count, leading directly to the observed runtime improvement.

These results suggest that the reduction in expected runtime achieved by QACG is driven jointly by fast QEC cycle times and by the ability to initialize a nontrivial low-energy spectral band on the quantum processor. Notably, the onset of this reduction occurs at  $n \approx 2^{12}$  in the  $\tau = 1 \text{ ns}$  regime, corresponding to a linear system with  $N \approx 2^{36}$  unknowns. At this scale, classical HPC systems begin to face severe memory-access constraints, whereas an integrated quantum-HPC platform can exploit early FTQC devices to complement state-of-the-art classical resources.

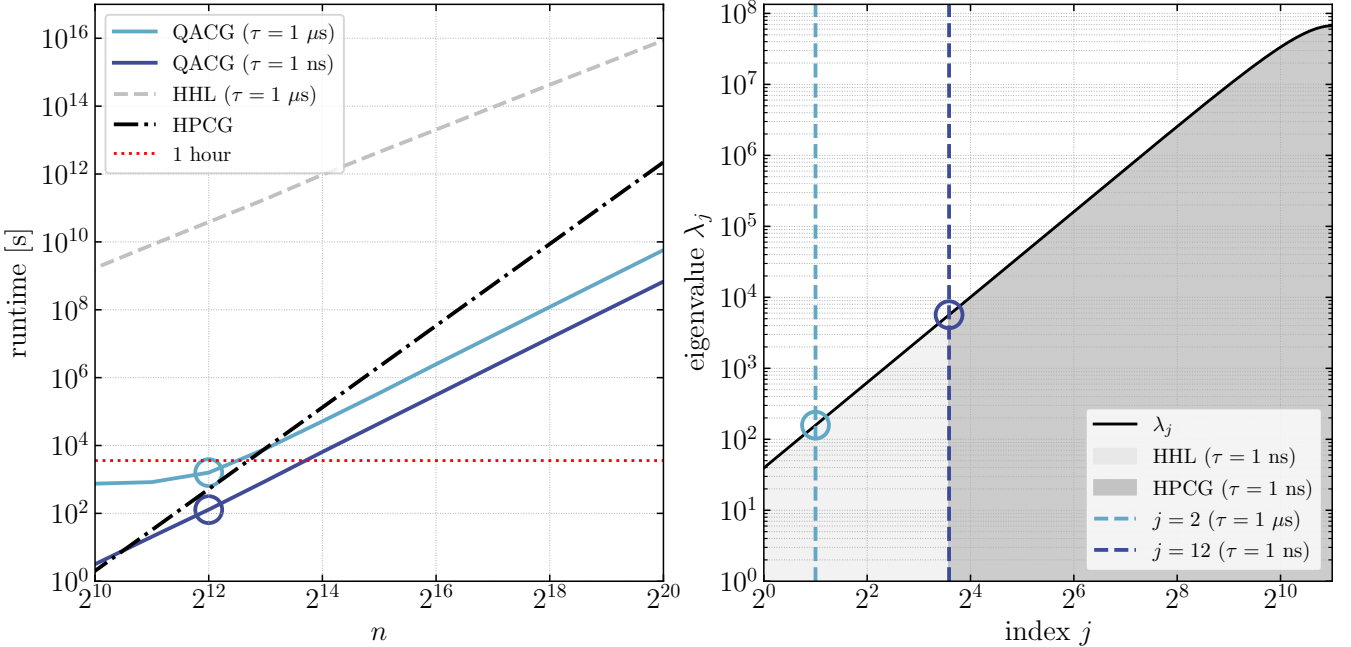


FIG. 6. Expected runtime comparison and spectral initialization behavior for CG, HHL, and runtime-optimized QACG applied to the 3D Poisson equation on an integrated quantum-HPC platform. Left: Expected runtime as a function of problem size  $n$  for classical HPCG, full HHL, and QACG with QEC cycle times  $\tau = 1 \mu\text{s}$  and  $\tau = 1 \text{ ns}$ . While HPCG remains faster than QACG at  $n \approx 2^{12}$  for  $\tau = 1 \mu\text{s}$ , QACG with  $\tau = 1 \text{ ns}$  achieves a lower expected runtime beyond this scale. Full HHL remains significantly slower due to its dependence on the full condition number and large fault-tolerant overheads. Right: Eigenvalue spectrum  $\{\lambda_j\}$  of the Poisson operator and the optimized spectral initialization window selected by QACG at  $n = 2^{12}$ . For  $\tau = 1 \mu\text{s}$ , the window remains at the spectral origin ( $j = 2$ ), providing negligible acceleration. In contrast, for  $\tau = 1 \text{ ns}$ , QACG initializes a broader low-energy subspace ( $j = 12$ ), enabling more effective suppression of classical residuals and a corresponding reduction in expected runtime.

## B. Resource estimation

In FIG. 7, we show the logical resource requirements for executing full HHL and runtime-optimized QACG on the STAR architecture (Definition 4). Specifically, we plot the number of logical qubits and logical gate counts required to implement HHL with  $\kappa' = \kappa$  and QACG with an optimized quantum condition number  $\kappa'$ , for two representative QEC cycle times,  $\tau = 1 \mu\text{s}$  and  $\tau = 1 \text{ ns}$ . The logical gate counts  $\mathcal{G}_H$ ,  $\mathcal{G}_S$ ,  $\mathcal{G}_{\text{CNOT}}$ , and  $\mathcal{G}_{R_Z}$  are evaluated using the expressions in Definition 8, with  $\kappa'$  selected by COBYQA through minimization of the expected runtime.

The left panel corresponds to the conservative setting  $\tau = 1 \mu\text{s}$ . Over the range of problem sizes considered, the gray points represent full HHL, while the light-blue points correspond to QACG. As expected, the logical qubit and gate requirements of full HHL increase rapidly with  $n$ , reflecting the direct dependence of the algorithm on the full condition number  $\kappa$ . In contrast, QACG exhibits a markedly reduced growth rate once the runtime-optimal  $\kappa'$  is substantially smaller than  $\kappa$ . This reduction arises because only a restricted low-energy spectral band is treated by the quantum subroutine, while the remaining spectral components are delegated to classical CG

refinement on the HPC system.

At representative scales highlighted by the dotted reference lines at  $n = 2^{14}$ , restricting the quantum subroutine to the optimized low-energy sector reduces the CNOT count by approximately from  $10^{16}$  to  $10^8$  relative to full HHL, while lowering the logical qubit requirement by roughly an order of magnitude. Across the full range shown, QACG consistently operates in a regime where both the qubit count and total logical gate counts are far below those required for executing HHL with  $\kappa' = \kappa$ . Among the individual gate types, the  $H$ ,  $R_Z$ , and CNOT counts exhibit similar scaling behavior, consistent with their dominant dependence on  $\kappa'$  in Definition 8, whereas the  $S$ -gate count remains subdominant throughout.

The right panel shows the corresponding resource estimates for a faster QEC cycle,  $\tau = 1 \text{ ns}$ . As expected, the logical gate and qubit counts themselves do not depend explicitly on  $\tau$ ; however, the reduced cycle time shifts the runtime-optimal crossover between QACG and classical HPCG to smaller problem sizes i.e.  $n = 2^{11}$ , as indicated by the dotted reference lines. In particular, the crossover is reached at lower values of the logical qubit count and total logical gate count than in the  $\tau = 1 \mu\text{s}$  case. Although the faster QEC cycle favors larger optimal values of  $\kappa'$  in the runtime analysis this does not

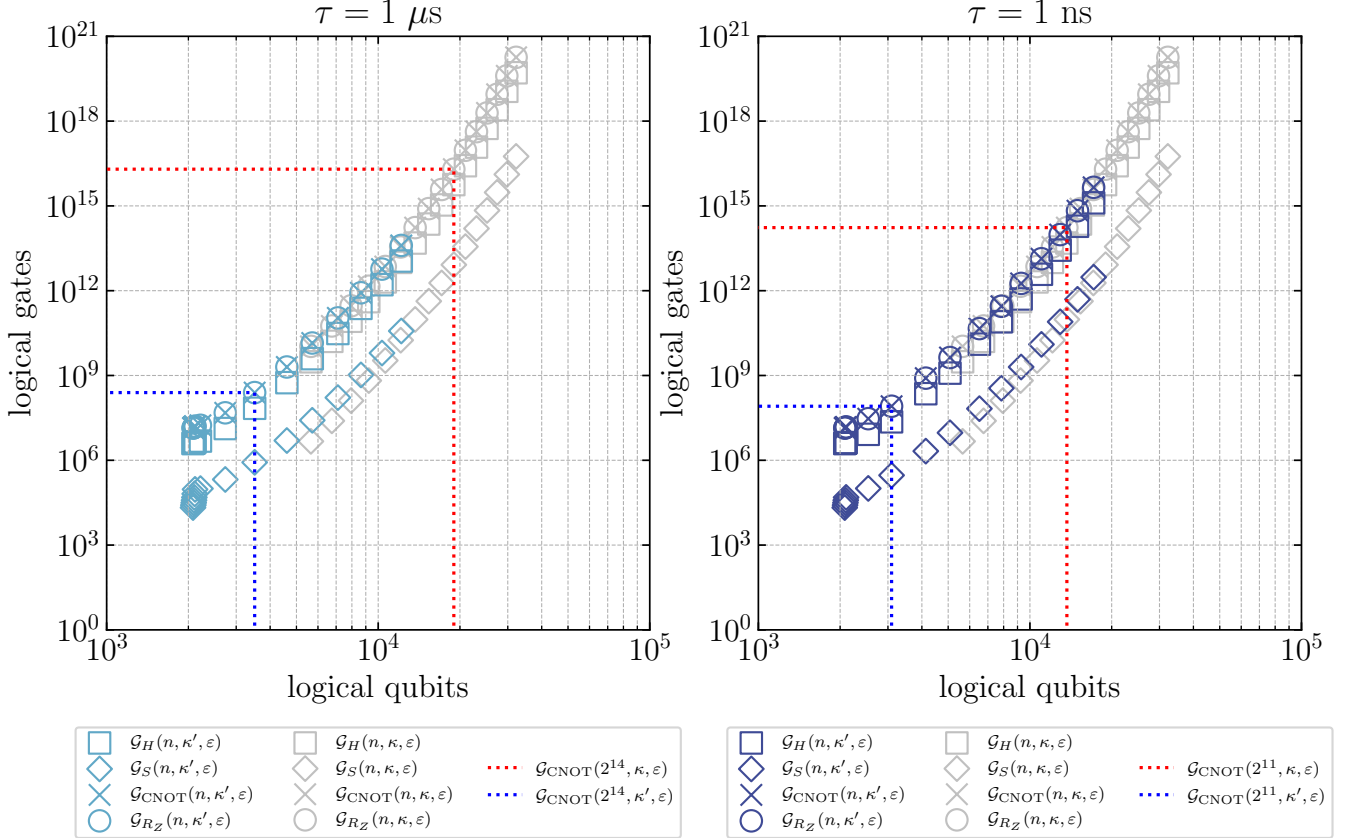


FIG. 7. Estimated logical qubit and gate requirements for full HHL and runtime-optimized QACG on the STAR architecture for the 3D Poisson equation. Gray markers correspond to full HHL implemented with the complete condition number  $\kappa$ , while colored markers show QACG using a runtime-optimized quantum condition number  $\kappa'$ . Left and right panels correspond to QEC cycle times  $\tau = 1 \mu\text{s}$  and  $\tau = 1 \text{ ns}$ , respectively. Dotted reference lines indicate the expected runtime crossover between QACG and HPCG. Although the logical qubit and gate counts are independent of  $\tau$ , a faster QEC cycle shifts the runtime-optimal crossover to smaller problem sizes, allowing QACG to achieve its advantage with fewer logical qubits and gates. Across both regimes, QACG reduces logical gate counts by several orders of magnitude relative to full HHL, while requiring substantially fewer logical qubits.

increase the required resources at the crossover point. Instead, QACG achieves its runtime advantage earlier, with substantially fewer logical qubits and gates. Even in this optimistic regime, the logical CNOT counts required by QACG reduced approximately from  $10^{14}$  to  $10^8$  relative to full HHL.

Finally, we emphasize that the substantial reduction in logical qubits and gate counts achieved by QACG is obtained by explicitly assuming that the remaining spectral components are processed on the HPC system via classical CG. This suggests that the optimization of the spectral initialization should be calibrated jointly against the capabilities of both the quantum device and the HPC platform. Such co-design is essential for maximizing overall resource utilization and performance in an integrated quantum–HPC platform.

### C. Numerical simulation for the 1D Poisson equation

To verify QACG (Algorithm 1), we numerically investigate the effect of spectral initialization on CG convergence for a 1D semiconductor device simulation. Here, spectral initialization serves as a classical surrogate for the output of the HHL algorithm [20], which encodes an approximate solution of  $Ax = b$  in the amplitudes of a quantum state through phase estimation with a limited number of ancilla qubits.

We consider the 1D Poisson equation for an abrupt p–n junction diode at thermal equilibrium [50]:

$$\frac{d^2V}{dz^2} = -\frac{\rho(V)}{\varepsilon_{\text{Si}}}, \quad (75)$$

where  $V(z)$  is the electrostatic potential,  $\varepsilon_{\text{Si}} = 1.05 \times 10^{-12} \text{ [F/cm]}$  is the silicon permittivity, and the charge

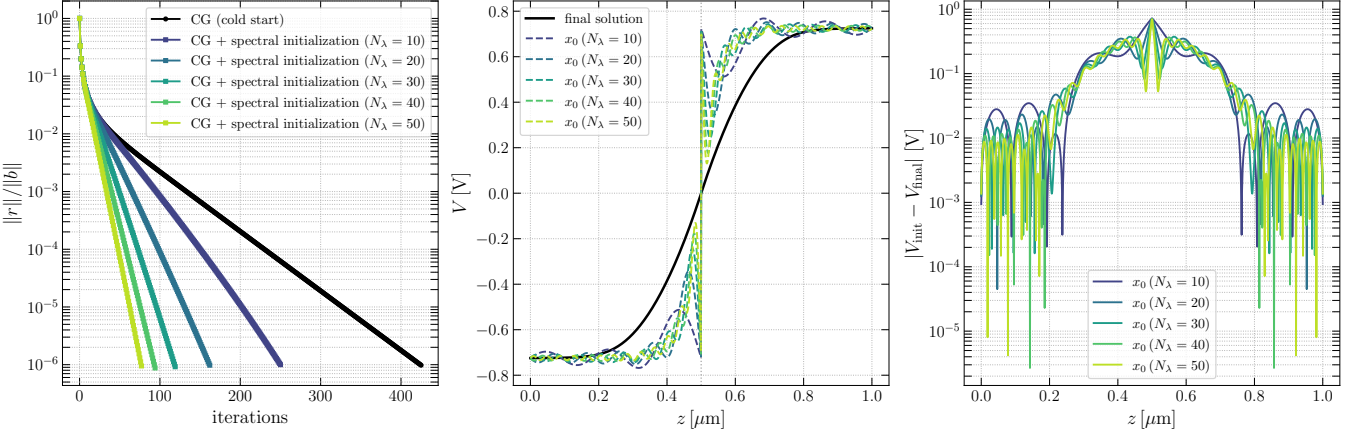


FIG. 8. Effect of spectral initialization on CG convergence for the p–n diode Poisson problem ( $n = 2^{10}$  grid points). Left: Relative residual versus iteration count for cold-start CG and CG with spectral initialization using  $N_\lambda \in \{10, 20, 30, 40, 50\}$  eigenvalues. Center: Comparison of the spectrally initialized potential profiles with the converged solution; the dashed lines show the initial guess  $V_{\text{init}}(z)$  obtained from (22). Right: Spatial error profile  $|V_{\text{init}} - V_{\text{final}}|$  of the initial guess, showing oscillatory behavior concentrated near the p–n junction.

density under Boltzmann statistics is given by

$$\rho(V) = e \left( N_D - N_A - n_i e^{V/U_T} + n_i e^{-V/U_T} \right), \quad (76)$$

with  $U_T = k_B T/e$  denoting the thermal voltage,  $n_i$  the intrinsic carrier density, and  $N_A$ ,  $N_D$  the acceptor and donor doping concentrations, respectively.

The simulation parameters are: temperature  $T = 300$  [K], symmetric doping  $N_A = N_D = 10^{16}$  [ $\text{cm}^{-3}$ ], bandgap energy  $E_g = 1.12$  [eV], device length  $L = 1$  [ $\mu\text{m}$ ], and  $n = 2^{10}$  interior grid points. The discretized system yields a tridiagonal Jacobian matrix  $A \in \mathbb{R}^{n \times n}$  that is SPD.

The HHL algorithm is assumed to construct an approximate solution by projecting onto the eigenspace of  $A$  via quantum phase estimation. When phase estimation uses  $n_\lambda$  ancilla qubits, only  $N_\lambda = 2^{n_\lambda}$  distinct eigenvalue bins are resolvable, effectively truncating the spectral representation to a limited number of eigenmodes. We model this spectral filtering classically by computing the truncated spectral inverse with (22). This initialization  $x_{(0)}$  serves as the starting point for subsequent CG iterations.

FIG. 8 presents the convergence behavior of CG with varying degrees of spectral initialization. The left panel shows the relative residual  $\|r\|/\|b\|$  as a function of iteration count. Starting from a cold (zero) initialization, CG requires 425 iterations to reach a relative tolerance of  $10^{-6}$ . In contrast, spectral initialization with  $N_\lambda \in \{10, 20, 30, 40, 50\}$  eigenvalues reduces the iteration count to  $\{250, 162, 119, 94, 77\}$ , respectively, demonstrating a consistent improvement with increasing spectral resolution.

The center panel of FIG. 8 compares the spectrally initialized potential profiles with the converged solution. While all initializations capture the qualitative shape of the built-in potential, larger  $N_\lambda$  yields closer approxi-

mations to the final solution. The right panel quantifies the spatial distribution of the initialization error  $|V_{\text{init}} - V_{\text{final}}|$ . The error exhibits oscillatory structure, with the largest deviations occurring near the p–n junction where the potential gradient is steepest. This behavior is consistent with the fact that low-frequency eigenmodes (small  $\lambda_k$ ) capture smooth, long-wavelength features, while the sharp junction transition requires higher-frequency components for accurate representation.

## VI. CONCLUSIONS AND OPEN PROBLEMS

In this work, we investigated an integrated quantum–HPC system for solving large-scale linear systems using CG, where a fault-tolerant quantum subroutine is used only to generate an initial guess. We formulated this strategy as QACG and showed, under explicit spectral and hardware assumptions, that quantum resources can be deployed in a restricted and targeted manner—without executing an end-to-end QLSA-style solver—while improving performance relative to a benchmark-calibrated classical baseline.

Our central observation is that the benefit of quantum assistance arises not from replacing CG, but from decomposing the workload across classical and quantum resources according to the spectral structure of the linear operator. By assigning a low-energy spectral window to the quantum initialization and delegating the remaining spectral content to classical CG, QACG exhibits a crossover regime in which both the estimated runtime and the quantum resources are reduced. In our model, this crossover depends jointly on the problem size, the quantum-side effective condition number  $\kappa'$ , the classical-side effective condition number  $\kappa''$ , and the assumed fault-tolerant clock speed, rather than on any single pa-

rameter.

Using time-complexity bounds and runtime/resource estimates based on the STAR architecture model, we found parameter regimes in which QACG outperforms the HPCG-calibrated classical baseline for the 3D Poisson problem. Importantly, the improvement does not rely on implementing a full inverse on the quantum device. Instead, restricting the quantum computation to a narrow spectral window reduces the logical gate counts and qubit requirements while providing a warm start that decreases the number of costly classical CG iterations. These results provide a concrete example of a regime beyond monolithic architecture in which classical and quantum resources cooperate to expand performance under the stated assumptions.

Several limitations should be emphasized. Most notably, we assumed that the quantum subroutine can hand over task-relevant classical information derived from the quantum state with negligible overhead. This assumption isolates the scaling behavior of the algorithmic decomposition but is not generally satisfied in realistic settings. Achieving practical impact will therefore require efficient interfaces between quantum and classi-

cal computations, including readout strategies that extract only task-relevant or compressed information rather than reconstructing the full quantum state. Promising directions include tighter integration between quantum phase estimation and Krylov-based workflows and hybrid schemes in which quantum routines provide spectral information that can be used to improve classical convergence.

Looking forward, the framework developed here suggests a pathway for extending the reach of classical HPC by integrating fault-tolerant quantum devices as cooperative accelerators within an integrated quantum–HPC system. Beyond the Poisson equation, it will be important to study broader CAE-relevant operator classes, including preconditioned systems and operators arising from more complex PDEs. Incorporating communication costs, synchronization overheads, and alternative fault-tolerant architectures will be necessary to refine quantitative predictions. More broadly, our results support the view that early, practical impact of fault-tolerant quantum computing in scientific and industrial workloads may come from hybrid schemes that align quantum subroutines with the specific bottlenecks of classical algorithms, rather than from fully quantum end-to-end solvers.

---

[1] Richard P. Feynman. Simulating physics with computers. *International Journal of Theoretical Physics*, 21(6):467–488, 1982.

[2] Peter W. Shor. Polynomial-time algorithms for prime factorization and discrete logarithms on a quantum computer. *SIAM Review*, 41(2):303–332, 1999.

[3] Artur Ekert and Richard Jozsa. Quantum computation and shor’s factoring algorithm. *Reviews of Modern Physics*, 68(3):733–753, 1996.

[4] Thomas Monz, Daniel Nigg, Esteban A. Martinez, Matthias F. Brandl, Philipp Schindler, Richard Rines, Shannon X. Wang, Isaac L. Chuang, and Rainer Blatt. Realization of a scalable shor algorithm. *Science*, 351(6277):1068–1070, 2016.

[5] Lov K. Grover. A fast quantum mechanical algorithm for database search. In *Proceedings of the Twenty-Eighth Annual ACM Symposium on Theory of Computing*, pages 212–219. ACM, 1996.

[6] Aamir Mandviwalla, Keita Ohshiro, and Bo Ji. Implementing grover’s algorithm on the ibm quantum computers. In *2018 IEEE International Conference on Big Data (Big Data)*, pages 2531–2537. IEEE, 2018.

[7] Daniel A. Lidar and Todd A. Brun. *Quantum Error Correction*. Cambridge University Press, 2013.

[8] Simon J. Devitt, William J. Munro, and Kae Nemoto. Quantum error correction for beginners. *Reports on Progress in Physics*, 76(7):076001, 2013.

[9] Joschka Roffe. Quantum error correction: an introductory guide. *Contemporary Physics*, 60(3):226–245, 2019.

[10] Rajeev Acharya, Dmitry A. Abanin, Laleh Aghababaie-Beni, Igor Aleiner, Trond I. Andersen, Markus Ansmann, Frank Arute, Kunal Arya, Abraham Asfaw, Nikita Astakhantsev, Juan Atalaya, Ryan Babbush, Dave Bacon, Brian Ballard, Joseph C. Bardin, Johannes Bausch, Andreas Bengtsson, Alexander Bilmes, Sam Blackwell, Sergio Boixo, Gina Bortoli, Alexandre Bourassa, Jenna Boavard, Leon Brill, Michael Broughton, David A. Browne, Brett Buechea, Bob B. Buckley, David A. Buell, Tim Burger, Brian Burkett, Nicholas Bushnell, Anthony Cabrera, Juan Campero, Hung-Shen Chang, Yu Chen, Zijun Chen, Ben Chiaro, Desmond Chik, Charina Chou, Jahan Claes, Agnetta Y. Cleland, Josh Cogan, Roberto Collins, Paul Conner, William Courtney, Alexander L. Crook, Ben Curtin, Sayan Das, Alex Davies, Laura De Lorenzo, Dripto M. Debroy, Sean Demura, Michel Devoret, Agustin Di Paolo, Paul Donohoe, Ilya Drozdov, Andrew Dunsworth, Clint Earle, Thomas Edlich, Alec Eickbusch, Aviv Moshe Elbag, Mahmoud Elzouka, Catherine Erickson, Lara Faoro, Edward Farhi, Vini- cius S. Ferreira, Leslie Flores Burgos, Ebrahim Forati, Austin G. Fowler, Brooks Foxen, Suhas Ganjam, Gonzalo Garcia, Robert Gasca, Élie Genois, William Giang, Craig Gidney, Dar Gilboa, Raja Gosula, Alejandro Grajales Dau, Dietrich Graumann, Alex Greene, Jonathan A. Gross, Steve Habegger, John Hall, Michael C. Hamilton, Monica Hansen, Matthew P. Harrigan, Sean D. Harrington, Francisco J. H. Heras, Stephen Heslin, Paula Heu, Oscar Higgott, Gordon Hill, Jeremy Hilton, George Holland, Sabrina Hong, Hsin-Yuan Huang, Ashley Huff, William J. Huggins, Lev B. Ioffe, Sergei V. Isakov, Justin Iveland, Evan Jeffrey, Zhang Jiang, Cody Jones, Stephen Jordan, Chaitali Joshi, Pavol Juhas, Dvir Kafri, Hui Kang, Amir H. Karamlou, Kostyantyn Kechedzhi, Julian Kelly, Trupti Khaire, Tanuj Khattar, Mostafa Khezri, Seon Kim, Paul V. Klimov, Andrey R. Klots, Bryce Kobrin, Pushmeet Kohli, Alexander N. Korotkov,

Fedor Kostritsa, Robin Kothari, Borislav Kozlovskii, John Mark Kreikebaum, Vladislav D. Kurilovich, Nathan Lacroix, David Landhuis, Tiano Lange-Dei, Brandon W. Langley, Pavel Laptev, Kim-Ming Lau, Loïck Le Guevel, Justin Ledford, Joonho Lee, Kenny Lee, Yuri D. Lensky, Shannon Leon, Brian J. Lester, Wing Yan Li, Yin Li, Alexander T. Lill, Wayne Liu, William P. Livingston, Aditya Locharla, Erik Lucero, Daniel Lundahl, Aaron Lunt, Sid Madhuk, Fionn D. Malone, Ashley Malone, Salvatore Mandrà, James Manyika, Leigh S. Martin, Orion Martin, Steven Martin, Cameron Maxfield, Jarrod R. McClean, Matt McEwen, Seneca Meeks, Anthony Megrant, Xiao Mi, Kevin C. Miao, Amanda Mieszala, Reza Molavi, Sebastian Molina, Shirin Montazeri, Alexis Morvan, Ramis Movassagh, Wojciech Mruczkiewicz, Ofer Naaman, Matthew Neeley, Charles Neill, Ani Nersisyan, Hartmut Neven, Michael Newman, Jiun How Ng, Anthony Nguyen, Murray Nguyen, Chia-Hung Ni, Murphy Yuezhen Niu, Thomas E. O'Brien, William D. Oliver, Alex Opremcak, Kristoffer Ottosson, Andre Petukhov, Alex Pizzuto, John Platt, Rebecca Potter, Orion Pritchard, Leonid P. Pryadko, Chris Quintana, Ganesh Ramachandran, Matthew J. Reagor, John Redding, David M. Rhodes, Gabrielle Roberts, Elliott Rosenberg, Emma Rosenfeld, Pedram Roushan, Nicholas C. Rubin, Negar Saei, Daniel Sank, Kannan Sankaragomathi, Kevin J. Satzinger, Henry F. Schurkus, Christopher Schuster, Andrew W. Senior, Michael J. Shearn, Aaron Shorter, Noah Shatty, Vladimir Shvarts, Shradhha Singh, Volodymyr Sivak, Jindra Skrzyn, Spencer Small, Vadim Smelyanskiy, W. Clarke Smith, Rolando D. Somma, Sofia Springer, George Sterling, Doug Strain, Jordan Suchard, Aaron Szasz, Alex Sztein, Douglas Thor, Alfredo Torres, M. Mert Torunbalci, Abeer Vaishnav, Justin Vargas, Sergey Vdovichev, Guifré Vidal, Benjamin Villalonga, Catherine Vollgraff Heidweiller, Steven Waltman, Shannon X. Wang, Brayden Ware, Kate Weber, Travis Weidel, Theodore White, Kristi Wong, Bryan W. K. Woo, Cheng Xing, Z. Jamie Yao, Ping Yeh, Bicheng Ying, Juhwan Yoo, Noureddin Yosri, Grayson Young, Adam Zalcman, Yaxing Zhang, Ningfeng Zhu, and Nicholas Zobrist. Quantum error correction below the surface code threshold. *Nature*, 638(8052):920–926, 2024.

[11] John Preskill. Quantum computing in the NISQ era and beyond. *Quantum*, 2:79, 2018.

[12] Keita Kanno, Masaya Kohda, Ryosuke Imai, Sho Koh, Kosuke Mitarai, Wataru Mizukami, and Yuya O. Nakagawa. Quantum-selected configuration interaction: Classical diagonalization of hamiltonians in subspaces selected by quantum computers, 2023.

[13] Javier Robledo-Moreno, Mario Motta, Holger Haas, Ali Javadi-Abhari, Petar Jurcevic, William Kirby, Simon Martiel, Kunal Sharma, Sandeep Sharma, Tomonori Shirakawa, et al. Chemistry beyond exact solutions on a quantum-centric supercomputer, 2024.

[14] Jeffery Yu, Javier Robledo-Moreno, Joseph T. Iosue, Luke Bertels, Daniel Claudino, Bryce Fuller, Peter Groszkowski, Travis S. Humble, Petar Jurcevic, William Kirby, et al. Quantum-centric algorithm for sample-based krylov diagonalization, 2025.

[15] Daniel Gottesman. Theory of fault-tolerant quantum computation. *Physical Review A*, 57(1):127–137, 1998.

[16] Peter W. Shor. Fault-tolerant quantum computation. In *Proceedings of the 37th Annual Symposium on Foundations of Computer Science*, pages 56–65. IEEE, 1996.

[17] John Preskill. Fault-tolerant quantum computation. In *Introduction to Quantum Computation and Information*. World Scientific, 1998.

[18] Dorit Aharonov and Michael Ben-Or. Fault-tolerant quantum computation with constant error. In *Proceedings of the Twenty-Ninth Annual ACM Symposium on Theory of Computing*, pages 176–188. ACM, 1997.

[19] Kentaro Yamamoto, Yuta Kikuchi, David Amaro, Ben Criger, Silas Dilkes, Ciarán Ryan-Anderson, Andrew Tranter, Joan M. Dreiling, Dan Gresh, Cameron Foltz, Michael Mills, Steven A. Moses, Peter E. Siegfried, Maxwell D. Urmey, Justin J. Burau, Aaron Hankin, Dominic Lucchetti, John P. Gaebler, Natalie C. Brown, Brian Neyenhuis, and David Muñoz Ramo. Quantum error-corrected computation of molecular energies, 2025.

[20] Aram W. Harrow, Avinatan Hassidim, and Seth Lloyd. Quantum algorithm for linear systems of equations. *Physical Review Letters*, 103(15):150502, 2009.

[21] Mario Motta, Kevin J. Sung, K. Birgitta Whaley, Martin Head-Gordon, and James Shee. Bridging physical intuition and hardware efficiency for correlated electronic states: the local unitary cluster jastrow ansatz for electronic structure. *Chemical Science*, 14(40):11213–11227, 2023.

[22] Jerry M. Chow. Quantum computing requires high-performance software. *Science*, 387(6736):eadt0019, 2025.

[23] Yutaro Akahoshi, Kazunori Maruyama, Hirotaka Oshima, Shintaro Sato, and Keisuke Fujii. Partially fault-tolerant quantum computing architecture with error-corrected clifford gates and space-time efficient analog rotations. *PRX Quantum*, 5(1):010337, 2024.

[24] Konstantinos Rallis, Ioannis Liliopoulos, Georgios D. Varsamis, Evangelos Tsipas, Ioannis G. Karafyllidis, Georgios Ch. Sirakoulis, and Panagiotis Dimitrakis. Interfacing quantum computing systems with high-performance computing systems: An overview, 2025.

[25] Eric Mansfield, Stefan Seegerer, Panu Vesanan, Jorge Echavarria, Burak Mete, Muhammad Nufail Farooqi, and Laura Schulz. First practical experiences integrating quantum computers with HPC resources: A case study with a 20-qubit superconducting quantum computer, 2025.

[26] Jonathan R. Shewchuk. An introduction to the conjugate gradient method without the agonizing pain. Technical report, Carnegie Mellon University, USA, 1994.

[27] Do Y. Kwak. V-cycle multigrid for cell-centered finite differences. *SIAM Journal on Scientific Computing*, 21(2):552–564, 1999.

[28] Shengtai Li. Comparison of refinement criteria for structured adaptive mesh refinement. *Journal of Computational and Applied Mathematics*, 233(12):3139–3147, 2010.

[29] Danial Dervovic, Mark Herbster, Peter Mountney, Simone Severini, Nári Usher, and Leonard Wossnig. Quantum linear systems algorithms: a primer, 2018.

[30] Mauro E. S. Morales, Lirandë Pira, Philipp Schleich, Kelvin Koor, Pedro C. S. Costa, Dong An, Alán Aspuru-Guzik, Lin Lin, Patrick Rebentrost, and Dominic W. Berry. Quantum linear system solvers: A survey of algorithms and applications, 2025.

[31] Pedro C. S. Costa, Dong An, Yuval R. Sanders, Yuan Su,

Ryan Babbush, and Dominic W. Berry. Optimal scaling quantum linear-systems solver via discrete adiabatic theorem. *PRX Quantum*, 3(4):040303, 2022.

[32] B. D. Clader, B. C. Jacobs, and C. R. Sprouse. Preconditioned quantum linear system algorithm. *Physical Review Letters*, 110(25):250504, 2013.

[33] Daan Camps, Lin Lin, Roel Van Beeumen, and Chao Yang. Explicit quantum circuits for block encodings of certain sparse matrices, 2023.

[34] E. Alper Yildirim and Stephen J. Wright. Warm-start strategies in interior-point methods for linear programming. *SIAM Journal on Optimization*, 12(3):782–810, 2002.

[35] Jordan Ash and Ryan P. Adams. On warm-starting neural network training. In *Advances in Neural Information Processing Systems*, volume 33, pages 3884–3894. Curran Associates, Inc., 2020.

[36] Daniel J. Egger, Jakub Mareček, and Stefan Woerner. Warm-starting quantum optimization. *Quantum*, 5:479, 2021.

[37] Zeyi Tao, Jindi Wu, Qi Xia, and Qun Li. LAWS: Look around and warm-start natural gradient descent for quantum neural networks. In *2023 IEEE International Conference on Quantum Software (QSW)*, pages 76–82. IEEE, 2023.

[38] Hang Zou, Martin Rahm, Anton Frisk Kockum, and Simon Olsson. Generative flow-based warm start of the variational quantum eigensolver. *npj Quantum Information*, 12(1), 2025.

[39] Felix Truger, Johanna Barzen, Marvin Bechtold, Martin Beisel, Frank Leymann, Alexander Mandl, and Vladimir Yussupov. Warm-starting and quantum computing: A systematic mapping study. *ACM Computing Surveys*, 56(9):229, 2024.

[40] Andrew M. Childs, Robin Kothari, and Rolando D. Somma. Quantum algorithm for systems of linear equations with exponentially improved dependence on precision. *SIAM Journal on Computing*, 46(6):1920–1950, 2017.

[41] Koichi Miyamoto and Hiroshi Ueda. Extracting a function encoded in amplitudes of a quantum state by tensor network and orthogonal function expansion. *Quantum Information Processing*, 22(6):239, 2023.

[42] Gumar Rendon and Stepan Smid. Preconditioned multivariate quantum solution extraction, 2026.

[43] Gumar Rendon. Exponentially improved constant in quantum solution extraction, 2025.

[44] Xinchi Huang, Hirofumi Nishi, Yoshifumi Kawada, Tomofumi Zushi, and Yu-ichiro Matsushita. Fourier space readout method for efficiently recovering functions encoded in quantum states, 2025.

[45] Giuliano Benenti and Giuliano Strini. Quantum simulation of the single-particle schrödinger equation. *American Journal of Physics*, 76(7):657–662, 2008.

[46] Andrew M. Childs and Jin-Peng Liu. Quantum spectral methods for differential equations. *Communications in Mathematical Physics*, 375(2):1427–1457, 2020.

[47] Mudassir Moosa, Thomas W. Watts, Yiyou Chen, Abhijat Sarma, and Peter L. McMahon. Linear-depth quantum circuits for loading fourier approximations of arbitrary functions. *Quantum Science and Technology*, 9(1):015002, 2023.

[48] Jack Dongarra, Michael A. Heroux, and Piotr Luszczek. High-performance conjugate-gradient benchmark: A new metric for ranking high-performance computing systems. *International Journal of High Performance Computing Applications*, 30(1), 2015.

[49] Linghang Kong, Fang Zhang, and Jianxin Chen. Benchmarking fault-tolerant quantum computing hardware via QLOPS, 2025.

[50] Arnout Beckers. Robust simulation of poisson's equation in a P–N diode down to 1  $\mu$ k, 2022.

[51] Almudena Carrera Vazquez, Ralf Hiptmair, and Stefan Woerner. Enhancing the quantum linear systems algorithm using richardson extrapolation. *ACM Transactions on Quantum Computing*, 3(1):1–37, 2022.

[52] Thomas Häner, Martin Roetteler, and Krysta M. Svore. Optimizing quantum circuits for arithmetic, 2018.

[53] Randall J. LeVeque. *Finite Difference Methods for Ordinary and Partial Differential Equations*. Society for Industrial and Applied Mathematics, 2007.

[54] Robert M. Gray. Toeplitz and circulant matrices: a review. *Communications in Information Theory*, 2(3):155–239, 2005.

[55] Wan-Hsuan Lin, Daniel Bochen Tan, and Jason Cong. Reuse-aware compilation for zoned quantum architectures based on neutral atoms, 2024.

[56] Refaat Ismail, I-Chi Chen, Chen Zhao, Ronen Weiss, Fangli Liu, Hengyun Zhou, Sheng-Tao Wang, Andrew Sornborger, and Milan Kornjača. Transversal STAR architecture for megaquop-scale quantum simulation with neutral atoms, 2025.

[57] Michael A. Nielsen and Isaac L. Chuang. *Quantum Computation and Quantum Information: 10th Anniversary Edition*. Cambridge University Press, Cambridge, 2010.

[58] Adriano Barenco, Charles H. Bennett, Richard Cleve, David P. DiVincenzo, Norman Margolus, Peter Shor, Tycho Sleator, John A. Smolin, and Harald Weinfurter. Elementary gates for quantum computation. *Physical Review A*, 52(5):3457–3467, 1995.

[59] Byeongyong Park and Doyeol Ahn. Reducing CNOT count in quantum fourier transform for the linear nearest-neighbor architecture. *Scientific Reports*, 13(1):8638, 2023.

[60] Mikko Möttönen, Juha J. Vartiainen, Ville Bergholm, and Martti M. Salomaa. Transformation of quantum states using uniformly controlled rotations, 2004.

[61] Alexander F. Shaw, Pavel Lougovski, Jesse R. Stryker, and Nathan Wiebe. Quantum algorithms for simulating the lattice schwinger model. *Quantum*, 4:306, 2020.

[62] Xiaonan Liu, Chenyan Zhao, Haoshan Xie, and Zhengyu Liu. Circuit simulation and optimization of quantum search algorithm. In *Proceedings of the 2022 6th International Conference on Electronic Information Technology and Computer Engineering*, pages 528–532. Association for Computing Machinery, 2023.

## ACKNOWLEDGMENTS

The authors are grateful to Yosuke Komiya for valuable discussions and insightful comments that greatly contributed to this work.

## Appendix A: Eigenvalue inversion using Richardson extrapolation

This appendix briefly summarizes the eigenvalue inversion procedure based on Richardson extrapolation introduced in Ref. [51]. Let  $A$  be a Hermitian matrix with eigenpairs  $\{(\lambda_j, |u_j\rangle)\}$  and condition number  $\kappa = \lambda_{\max}/\lambda_{\min}$ . Within the HHL framework, after quantum phase estimation one obtains an  $n_\lambda$ -qubit register encoding a fixed-point approximation  $\tilde{\lambda}_j$  of each eigenvalue. The inversion step aims to produce an ancilla amplitude proportional to  $\tilde{\lambda}_j^{-1}$ , while controlling the contribution of this operation to the total algorithmic error.

Rather than implementing a direct controlled rotation with angle proportional to  $\tilde{\lambda}_j^{-1}$ , Ref. [51] approximates the angle function

$$f(x) = \arcsin\left(\frac{c}{x}\right), \quad (\text{A1})$$

where  $x$  denotes the integer-valued eigenvalue estimate stored in the register and the constant  $c > 0$  is chosen such that  $0 < c/x < 1$  over the relevant spectral range. The domain of  $x$  is taken to be  $[a, 2^{n_\lambda} - 1]$ , where  $a$  is a cutoff introduced to control the approximation error near the smallest eigenvalues.

The interval  $[a, 2^{n_\lambda} - 1]$  is partitioned into a union of exponentially growing subintervals,

$$[a_1, a_2] \cup [a_2, a_3] \cup \dots \cup [a_M, a_{M+1}], \quad (\text{A2})$$

with  $a_1 = a$  and  $a_{\ell+1} = 5a_\ell$ . The total number of intervals is therefore

$$M = \left\lceil \log_5 \left( \frac{2^{n_\lambda} - 1}{a} \right) \right\rceil. \quad (\text{A3})$$

On each subinterval, the function  $f$  is approximated by a Chebyshev interpolating polynomial of degree  $d$ . Richardson extrapolation is used to cancel leading-order truncation errors, yielding a piecewise polynomial approximation whose uniform error satisfies

$$\|f - p_f\|_{L^\infty} \leq \varepsilon_C, \quad (\text{A4})$$

where  $\varepsilon_C$  denotes the target approximation accuracy of the angle function.

Ref. [51] shows that choosing

$$\varepsilon_C = \frac{\varepsilon}{2(2\kappa^2 - \varepsilon)}, \quad (\text{A5})$$

together with an eigenvalue register size

$$n_\lambda = 3 \left\lceil \log\left(\frac{2(2\kappa^2 - \varepsilon)}{\varepsilon} + 1\right) \right\rceil, \quad (\text{A6})$$

ensures that the contribution of the inversion step to the final HHL solution error is at most  $\varepsilon$ . Under these choices, the polynomial degree required to achieve the

above uniform bound can be estimated using analytic continuation of  $f$  to a Bernstein ellipse. An explicit bound given in Ref. [51] is

$$d = \left\lceil \log\left(1 + \frac{16.23\sqrt{\ln^2(r) + (\pi/2)^2}\kappa(2\kappa - \varepsilon)}{\varepsilon}\right) \right\rceil, \quad (\text{A7})$$

where the ellipse parameter  $r > 1$  depends on the ratio  $c/a$ . This yields the asymptotic scaling

$$d = \mathcal{O}\left(\log\left(\frac{\kappa^2}{\varepsilon}\right) + \log\log\left(\frac{\kappa^2}{\varepsilon}\right)\right). \quad (\text{A8})$$

The polynomial approximation  $p_f$  is evaluated reversibly, for example using a reversible Horner scheme [52], to compute an angle  $y_j \approx f(\tilde{\lambda}_j)$  from the eigenvalue register. A controlled  $R_Y$  rotation acting on an ancilla qubit then implements the standard HHL inversion primitive,

$$|0\rangle \mapsto \sqrt{1 - \frac{c^2}{\tilde{\lambda}_j^2}}|0\rangle + \frac{c}{\tilde{\lambda}_j}|1\rangle, \quad (\text{A9})$$

up to an error bounded by  $\varepsilon$  with the above parameter choices. In this way, the Richardson–Chebyshev construction replaces the direct inversion step by a controlled functional approximation with polylogarithmic dependence on  $1/\varepsilon$ , while maintaining explicit control over the condition-number dependence of the eigenvalue inversion subroutine, as established in Ref. [51].

## Appendix B: Resource estimation

In the following, we define some properties of the Poisson equation and derive the space and gate complexity.

### 1. Properties of the Poisson equation

**Definition 5** (Discrete Laplacian with periodic boundary conditions). *Let  $\Omega = (0, 1)$  and discretize on a uniform grid with spacing  $h = 1/n$  and grid points  $x_j = jh$  for  $j = 0, 1, \dots, n - 1$ . Define the 1D periodic discrete Laplacian  $L \in \mathbb{R}^{n \times n}$  by*

$$L = \frac{1}{h^2} \begin{bmatrix} 2 & -1 & 0 & \cdots & 0 & -1 \\ -1 & 2 & -1 & \ddots & & 0 \\ 0 & -1 & 2 & \ddots & \ddots & \vdots \\ \vdots & \ddots & \ddots & \ddots & -1 & 0 \\ 0 & & \ddots & -1 & 2 & -1 \\ -1 & 0 & \cdots & 0 & -1 & 2 \end{bmatrix}. \quad (\text{B1})$$

Equivalently,  $L$  is circulant with stencil  $(-1, +2, -1)/h^2$  and wrap-around couplings enforcing periodicity.

**Lemma 2** (Eigenvalues and Fourier diagonalization). *Let  $F$  be the  $n \times n$  discrete Fourier transform (DFT) matrix. Then*

$$L = F^\dagger \Lambda F, \quad \Lambda = \text{diag}(\lambda_0, \lambda_1, \dots, \lambda_{n-1}), \quad (\text{B2})$$

with eigenvalues

$$\lambda_k = \frac{4}{h^2} \sin^2 \left( \frac{\pi k}{n} \right), \quad k = 0, 1, \dots, n-1. \quad (\text{B3})$$

In particular,  $\lambda_0 = 0$  and  $L$  is singular.

*Proof.* Consider the standard second-order central finite-difference approximation of the 1D Laplacian on a uniform grid with spacing  $h$  under periodic boundary conditions with [Definition 5](#). In this setting, the discrete Laplacian is represented by a circulant matrix whose first row is given by  $(2, -1, 0, \dots, 0, -1)/h^2$  [\[53\]](#). It is a well-known result in linear algebra that circulant matrices are diagonalized by the discrete Fourier transform, and that their eigenvalues are obtained as the discrete Fourier transform of the first row [\[54\]](#). Applying this general result to the present case, the eigenvalues of the discrete Laplacian are explicitly given by

$$\lambda_k = \frac{1}{h^2} \left( 2 - e^{2\pi i k/N} - e^{-2\pi i k/N} \right) \quad (\text{B4})$$

$$= \frac{4}{h^2} \sin^2 \left( \frac{\pi k}{N} \right), \quad k = 0, 1, \dots, n-1, \quad (\text{B5})$$

with the corresponding eigenvectors given by the discrete Fourier modes.  $\square$

**Definition 6** (Zero-mean subspace and restricted inverse). *Define the zero-mean subspace*

$$\mathcal{H}_0 := \left\{ v \in \mathbb{R}^n : \sum_{j=0}^{n-1} v_j = 0 \right\}. \quad (\text{B6})$$

We consider the Poisson system  $Lx = b$  under the compatibility condition  $b \in \mathcal{H}_0$ . The solution is defined up to an additive constant; we select the zero-mean solution  $x \in \mathcal{H}_0$ . Equivalently, we use the inverse of  $L$  restricted to  $\mathcal{H}_0$  (or the Moore–Penrose pseudoinverse on  $\mathcal{H}_0$ ).

**Lemma 3** (Effective condition number on  $\mathcal{H}_0$ ). *On  $\mathcal{H}_0$  with [Definition 6](#), the smallest nonzero eigenvalue is  $\lambda_1$  and the largest eigenvalue is  $\lambda_{\max}$  (for even  $n$ , achieved at  $k = n/2$ ). Hence the effective condition number of  $L$  restricted to  $\mathcal{H}_0$  satisfies*

$$\kappa_{\mathcal{H}_0}(L) = \frac{\lambda_{\max}}{\lambda_1} = \frac{1}{\sin^2(\pi/n)} = \Theta(n^2). \quad (\text{B7})$$

**Lemma 4** (Sparsity of the discrete Laplacian in [Definition 5](#)). *For the matrix  $A \in \mathbb{R}^{N \times N}$  arising from [Definition 2](#) with  $N = n^3$  and the 7-point stencil,*

$$\max_i \text{nnz}(\text{row } i) = 7. \quad (\text{B8})$$

*Proof.* Each interior grid point couples to its 6 nearest neighbors plus itself, yielding 7 nonzeros per row. On boundary strata, the counts may be reduced depending on the boundary-condition treatment, while the maximal per-row count remains 7.  $\square$

## 2. Space complexity of HHL

In this and the following section, we use  $n$  to denote the number of qubits, such that the system dimension is  $N = 2^n$ . This convention differs from earlier sections of the paper, where  $n$  denotes the number of unknowns per spatial dimension in the discretized Poisson equation. When referring to the Poisson problem, the distinction is explicit through the use of  $N = n^3$  for the total number of degrees of freedom. Throughout the present discussion of QLSA and HHL complexity,  $n$  should therefore be interpreted exclusively as the logarithmic system-size parameter  $n = \log_2 N$ , consistent with standard conventions in quantum algorithm analysis.

We estimate the space complexity of HHL by accounting for all qubit registers that may be simultaneously active during the algorithm, with particular attention to ancillary qubits required by arithmetic subroutines and by amplitude amplification.

The system register representing the 3D Laplacian  $A$  consists of  $3n$  qubits. Quantum phase estimation (QPE) introduces an  $n_\lambda$ -qubit eigenvalue register, where  $n_\lambda$  is determined by the precision required to resolve eigenvalues down to  $\Theta(1/\kappa)$ . In addition, HHL uses a single flag qubit to implement the eigenvalue-dependent rotation and postselection.

The dominant ancillary overhead arises from the eigenvalue-inversion step, which we implement using the parallel piecewise-polynomial evaluation circuit of [\[52\]](#). As stated in that resource estimate, the polynomial-evaluation circuit requires

$$\mathcal{S}_{\text{pp}}(n_\lambda, d, M) = (d+1)n_\lambda + \lceil \log_2 M \rceil + 1 \quad (\text{B9})$$

qubits in total, including the  $n_\lambda$ -qubit input register holding the eigenvalue. Therefore, beyond the eigenvalue register itself, the arithmetic introduces an additional workspace of

$$dn_\lambda + \lceil \log_2 M \rceil + 1 \quad (\text{B10})$$

qubits. Here  $d$  is the polynomial degree and  $M$  is the number of piecewise intervals, both fixed by the inversion accuracy requirements and already determined by the gate-complexity analysis.

A further source of ancillary qubits appears in the amplitude-amplification step. The diffusion operator  $U_0$  contains a multi-controlled  $X$  gate with  $k = 3n + n_\lambda$  control qubits acting on a target qubit. By [Lemma 8](#), an exact implementation of this MCX gate requires  $k - 2 = 3n + n_\lambda - 2$  ancilla qubits. In our construction, the target of this MCX can be taken to be the existing flag qubit, so no additional target qubit is required.

Putting these components together, a conservative upper bound on the peak number of qubits required by a single-shot HHL execution is obtained by assuming that the arithmetic workspace and the MCX ancillas are simultaneously allocated. Under this assumption, the peak qubit count is

$$\mathcal{S} \approx 3n + n_\lambda + 1 + (dn_\lambda + \lceil \log_2 M \rceil + 1) + (3n + n_\lambda - 2), \quad (\text{B11})$$

which scales as

$$\mathcal{S} = 6n + 2n_\lambda + dn_\lambda + \lceil \log_2 M \rceil + \mathcal{O}(1). \quad (\text{B12})$$

This bound is intentionally conservative. The eigenvalue-inversion arithmetic and the diffusion operator  $U_0$  are not executed concurrently, and on architectures that allow dynamic reuse of qubits, such as neutral-atom platforms [\[55, 56\]](#), the workspace allocated for polynomial evaluation may be recycled as ancillas for the MCX gate.

Throughout,  $n_\lambda$ ,  $d$ , and  $M$  are not independent parameters but are fixed by the precision and condition-number requirements of HHL, and are therefore determined consistently by the gate-complexity analysis.

For comparison, a classical CG solver on an integrated quantum-HPC system requires storing multiple  $\mathcal{O}(N)$ -sized vectors for the solution, residual, and search directions (with  $N = 2^{3n}$  for the same 3D discretization), whereas the quantum space cost scales only with the register sizes  $3n$  and  $n_\lambda$ , highlighting that the memory bottleneck shifts from vector storage to algorithmic workspace.

### 3. Gate complexity of HHL

Here we present the resource estimation procedure for our HHL implementation over the [Definition 4](#) gate set. Our approach decomposes HHL into a small number of well-defined circuit blocks, for which explicit gate complexities can be derived: (i) preparation of the right-hand-side vector using the FSL, (ii) QPE for eigenvalue estimation of the Laplacian-generated unitary, and (iii) eigenvalue inversion implemented as a controlled rotation driven by arithmetic, realized through piecewise-polynomial evaluation. These components are then assembled into a single-shot HHL cost, after which we incorporate the repetition overhead arising from amplitude amplification, following the methodology of [\[51\]](#).

Throughout this appendix,  $\mathcal{G}$  denotes exact logical gate counts over the set  $\{H, S, \text{CNOT}, R_Z\}$ .

The resource estimation proceeds by decomposing HHL into the following components:

- Evaluation assumptions and methodology.** The dominant contributions to the logical cost arise from the FSL, QPE, and the eigenvalue inversion. Other operations, such as `ClassicalDecode`, are not resolved explicitly in the gate count and are treated as subleading.
- Fourier series loader.** The cost of state preparation is accounted for using the explicit  $(n, m)$ -dependent gate complexities derived above, where  $m$  denotes the truncation order of the Fourier series and  $n$  is the per-dimension problem-size parameter.
- Quantum phase estimation.** The gate complexity of QPE is taken from [Lemma 12](#), using an  $n_\lambda$ -qubit eigenvalue register. Here,  $n$  again denotes the per-dimension problem-size parameter, and the Laplacian acts on  $3n$  qubits via the constructions detailed in [Lemma 11–Lemma 12](#).
- Eigenvalue inversion.** The eigenvalue-dependent inversion is costed using a Toffoli-dominated arithmetic estimate based on the parallel piecewise-polynomial evaluation scheme of [\[52\]](#), converted to STAR gates using [Lemma 6](#). The parameters  $(d, p, M)$  follow the definitions introduced above and depend on  $(n_\lambda, \kappa, \varepsilon)$  as specified in the eigenvalue-inversion analysis.

In the following, we summarize the basic gates and circuit components expressed over the gate set  $\{H, S, \text{CNOT}, R_Z\}$ .

**Lemma 5** (*T*-gate complexity). *Under the STAR gate set  $\{H, S, \text{CNOT}, R_Z\}$ , the  $T$  gate can be implemented exactly using a single  $R_Z$  gate. In particular,*

$$\mathcal{G}_{R_Z}(T) = 1. \quad (\text{B13})$$

*Proof.* The  $T$  gate is defined as

$$T = \begin{pmatrix} 1 & 0 \\ 0 & e^{i\pi/4} \end{pmatrix}. \quad (\text{B14})$$

The  $R_Z$  gate is given by

$$R_Z(\theta) = \begin{pmatrix} e^{-i\theta/2} & 0 \\ 0 & e^{i\theta/2} \end{pmatrix}. \quad (\text{B15})$$

Setting  $\theta = \pi/4$  yields

$$R_Z(\pi/4) = e^{-i\pi/8} \begin{pmatrix} 1 & 0 \\ 0 & e^{i\pi/4} \end{pmatrix}. \quad (\text{B16})$$

Up to a global phase, this is  $T$ , so one  $R_Z$  gate implements  $T$  exactly.  $\square$

**Lemma 6** (Toffoli gate complexity). *Under the STAR gate set  $\{H, S, CNOT, R_Z\}$ , the Toffoli gate admits an exact decomposition with the following gate complexities:*

$$\begin{aligned}\mathcal{G}_{CNOT} &= 7, \\ \mathcal{G}_H &= 2, \\ \mathcal{G}_{R_Z} &= 7.\end{aligned}\tag{B17}$$

*Proof.* A standard exact decomposition of the Toffoli gate uses Clifford and  $T$  gates with gate counts [57]

$$\begin{aligned}\mathcal{G}_{CNOT} &= 7, \\ \mathcal{G}_H &= 2, \\ \mathcal{G}_T &= 3, \\ \mathcal{G}_{T^\dagger} &= 4.\end{aligned}\tag{B18}$$

By Lemma 5, each  $T$  or  $T^\dagger$  can be implemented (up to a global phase) by a single  $R_Z$  gate. Therefore

$$\mathcal{G}_{R_Z} = \mathcal{G}_T + \mathcal{G}_{T^\dagger} = 7,\tag{B19}$$

while the CNOT and Hadamard counts are unchanged.  $\square$

**Lemma 7** (Controlled Hadamard gate complexity). *Under the STAR gate set  $\{H, S, CNOT, R_Z\}$ , the controlled-Hadamard (CH) gate admits an exact decomposition with gate complexities*

$$\begin{aligned}\mathcal{G}_{CNOT} &= 1, \\ \mathcal{G}_S &= 2, \\ \mathcal{G}_H &= 2, \\ \mathcal{G}_{R_Z} &= 2.\end{aligned}\tag{B20}$$

*Proof.* A general controlled single-qubit unitary gate  $CU$  admits an exact decomposition of the form

$$CU = (I \otimes A) \cdot \text{CNOT} \cdot (I \otimes B) \cdot \text{CNOT} \cdot (I \otimes C),\tag{B21}$$

where the single-qubit unitaries  $A, B, C$  satisfy  $ABC = I$  and  $U = AXBXC$  up to a global phase. For the Hadamard gate, one valid exact factorization is

$$H = S H R_Z(\pi/2) X R_Z(-\pi/2) H S^\dagger,\tag{B22}$$

where the phase gates  $S$  and the  $R_Z$  rotations belong to the STAR gate set. Substituting this decomposition into the standard controlled-unitary construction yields an exact implementation of the controlled-Hadamard gate. All other contributions reduce to identities or cancel due to the constraint  $ABC = I$ . This establishes the stated gate complexities.  $\square$

**Lemma 8** (Multi-controlled  $X$  gate complexity). *Let  $k \geq 3$ . A multi-controlled  $X$  (MCX) gate with  $k$  control qubits and one target qubit admits an exact implementation over the STAR gate set  $\{H, S, CNOT, R_Z\}$  using*

$k - 2$  ancilla qubits, with gate complexities

$$\begin{aligned}\mathcal{G}_{CNOT} &= 56(k - 5), \\ \mathcal{G}_H &= 16(k - 5), \\ \mathcal{G}_{R_Z} &= 56(k - 5).\end{aligned}\tag{B23}$$

*Proof.* Barenco et al. [58] show that a  $k$ -controlled  $X$  gate can be implemented exactly using

$$\mathcal{G}_{\text{Toffoli}} = 8(k - 5)\tag{B24}$$

Toffoli gates and  $k - 2$  ancilla qubits. By Lemma 6, each Toffoli has STAR gate complexities

$$\begin{aligned}\mathcal{G}_{CNOT} &= 7, \\ \mathcal{G}_H &= 2, \\ \mathcal{G}_{R_Z} &= 7.\end{aligned}\tag{B25}$$

Multiplying by  $8(k - 5)$  yields

$$\begin{aligned}\mathcal{G}_{CNOT} &= 56(k - 5), \\ \mathcal{G}_H &= 16(k - 5), \\ \mathcal{G}_{R_Z} &= 56(k - 5).\end{aligned}\tag{B26}$$

$\square$

**Lemma 9** (Gate complexity of QFT). *Consider implementing the  $n$ -qubit quantum Fourier transform with gate-set defined by Definition 4. The implementation requires*

$$\begin{aligned}\mathcal{G}_H &= n, \\ \mathcal{G}_{CNOT} &= n(n + 1), \\ \mathcal{G}_{R_Z} &= n(n + 1).\end{aligned}\tag{B27}$$

*Proof.* The conventional  $n$ -qubit QFT uses [59]

$$\begin{aligned}\mathcal{G}_H &= n, \\ \mathcal{G}_{CR_Z} &= \frac{n(n + 1)}{2}.\end{aligned}\tag{B28}$$

An exact decomposition of a controlled- $R_Z$  gate over  $\{H, S, \text{CNOT}, R_Z\}$  satisfies

$$\mathcal{G}_{CR_Z} = 2\mathcal{G}_{CNOT} + 2\mathcal{G}_{R_Z},\tag{B29}$$

so the controlled- $R_Z$  count implies  $\mathcal{G}_{CNOT} = n(n + 1)$  and  $\mathcal{G}_{R_Z} = n(n + 1)$ .  $\square$

*a. Cost of state preparation* We decompose the cost into contributions from the quantum Fourier transforms, from the coefficient-loading unitary at truncation order  $m$  implemented via a cascaded entangler (in 3D), and from the entangling CNOT ladders between the  $(m + 1)$ -qubit loader register and the remaining  $n - m - 1$  qubits in each dimension [47].

Since our FSL circuit contains three inverse QFT

blocks, their total contribution is

$$\begin{aligned}\mathcal{G}_H^{(i)} &= 3n, \\ \mathcal{G}_{\text{CNOT}}^{(i)} &= 3n(n+1), \\ \mathcal{G}_{R_Z}^{(i)} &= 3n(n+1).\end{aligned}\quad (\text{B30})$$

by [Lemma 9](#). The coefficient-loading unitary is realized using the standard uniformly-controlled-rotation  $U_c$  (cascaded entangler) [60]. For  $m$  target qubits this construction requires

$$\begin{aligned}N_{\text{CNOT}}(m) &= 2^{m+2} - 4m - 4, \\ N_{\text{rot}}(m) &= 2^{m+2} - 5,\end{aligned}\quad (\text{B31})$$

where  $N_{\text{rot}}$  denotes the total number of single-qubit rotations appearing as  $R_y(\cdot)$  and  $R_z(\cdot)$ . In particular, the uniformly-controlled construction contains

$$\begin{aligned}N_{R_y}(m) &= 2^{m+1} - 2, \\ N_{R_z}(m) &= 2^{m+1} - 3,\end{aligned}\quad (\text{B32})$$

so that  $N_{R_y}(m) + N_{R_z}(m) = N_{\text{rot}}(m)$ .

To express the circuit over [Definition 4](#), we rewrite each  $R_y$  rotation using the Clifford+ $R_Z$  identity

$$R_y(\theta) = S H R_z(\theta) H S^\dagger, \quad (\text{B33})$$

which introduces one  $R_Z(\theta)$  gate and Clifford gates only. Therefore, a single cascaded entangler contributes

$$\begin{aligned}\mathcal{G}_H^{\text{CE}}(m) &= 2N_{R_y}(m) = 2^{m+2} - 4, \\ \mathcal{G}_S^{\text{CE}}(m) &= 2N_{R_y}(m) = 2^{m+2} - 4, \\ \mathcal{G}_{\text{CNOT}}^{\text{CE}}(m) &= N_{\text{CNOT}}(m) = 2^{m+2} - 4m - 4, \\ \mathcal{G}_{R_Z}^{\text{CE}}(m) &= N_{\text{rot}}(m) = 2^{m+2} - 5.\end{aligned}\quad (\text{B34})$$

In the 3D FSL, the cascaded entangler is implemented independently in each dimension, so the total cascaded-entangler contribution is

$$\begin{aligned}\mathcal{G}_H^{(ii)}(m) &= 3\mathcal{G}_H^{\text{CE}}(m) = 3(2^{m+2} - 4), \\ \mathcal{G}_S^{(ii)}(m) &= 3\mathcal{G}_S^{\text{CE}}(m) = 3(2^{m+2} - 4), \\ \mathcal{G}_{\text{CNOT}}^{(ii)}(m) &= 3\mathcal{G}_{\text{CNOT}}^{\text{CE}}(m) = 3(2^{m+2} - 4m - 4), \\ \mathcal{G}_{R_Z}^{(ii)}(m) &= 3\mathcal{G}_{R_Z}^{\text{CE}}(m) = 3(2^{m+2} - 5).\end{aligned}\quad (\text{B35})$$

Finally, in each dimension the  $(m+1)$ -qubit loader register is connected to the remaining  $n-m-1$  qubits via a CNOT ladder in each direction, contributing

$$\mathcal{G}_{\text{CNOT}}^{(\text{ladder})}(m) = n - m - 1 \quad (\text{B36})$$

CNOT gates per dimension, hence

$$\mathcal{G}_{\text{CNOT}}^{(iii)}(m) = 3(n - m - 1). \quad (\text{B37})$$

Summing the QFT, 3D cascaded-entangler, and CNOT-ladder contributions gives the gate complexity as a function of  $(n, m)$ :

$$\begin{aligned}\mathcal{G}_H^{\text{FSL}}(n, m) &= \mathcal{G}_H^{(i)} + \mathcal{G}_H^{(ii)}(m), \\ \mathcal{G}_S^{\text{FSL}}(n, m) &= \mathcal{G}_S^{(ii)}(m), \\ \mathcal{G}_{\text{CNOT}}^{\text{FSL}}(n, m) &= \mathcal{G}_{\text{CNOT}}^{(i)} + \mathcal{G}_{\text{CNOT}}^{(ii)}(m) + \mathcal{G}_{\text{CNOT}}^{(iii)}(m), \\ \mathcal{G}_{R_Z}^{\text{FSL}}(n, m) &= \mathcal{G}_{R_Z}^{(i)} + \mathcal{G}_{R_Z}^{(ii)}(m).\end{aligned}\quad (\text{B38})$$

The truncation order  $m$  fixes the approximation accuracy of the Fourier series independently of any error parameter  $\varepsilon$ , so no additional  $\varepsilon$ -dependent factor appears in these gate counts.

*b. Cost of quantum phase estimation* We recursively construct the gate complexity of QPE. We begin by defining the gate complexity of the diagonal unitary matrix as follows.

**Lemma 10** (Gate complexity of the diagonal unitary matrix). *Consider implementing the  $n$ -qubit diagonal unitary matrix of the form  $e^{-i\lambda}$  where  $\lambda = \xi^2$  is a quadratic function with a gate-set defined by [Definition 4](#). The implementation requires*

$$\begin{aligned}\mathcal{G}_{\text{CNOT}} &= \frac{(n+1)(n-2)}{2}, \\ \mathcal{G}_{R_Z} &= \frac{n(n-1)}{2}.\end{aligned}\quad (\text{B39})$$

*Proof.* The stated counts follow from Ref. [61], which gives

$$\begin{aligned}\mathcal{G}_{\text{CNOT}} &= \frac{(\eta+2)(\eta-1)}{2}, \\ \mathcal{G}_{R_Z} &= \frac{\eta(\eta+1)}{2},\end{aligned}\quad (\text{B40})$$

with  $\eta = n - 1$ .  $\square$

**Lemma 11** (Gate complexity of  $\text{CU}^k$  gate). *Consider implementing the controlled unitary  $\text{CU}^k$  with  $U$  generated by a (3D) Laplacian defined by [Definition 5](#) (acting on  $3n$  qubits) on a partially-fault-tolerant quantum computer with gate-set [Definition 4](#). If  $U^k$  is realized by  $k$  sequential applications of  $U$  (as in standard QPE where  $k = 2^j$ ), then the implementation requires*

$$\begin{aligned}\mathcal{G}_H &= k(15n^2 + 21n - 6), \\ \mathcal{G}_S &= 12kn, \\ \mathcal{G}_{\text{CNOT}} &= k\left(\frac{135n^2}{2} + \frac{93n}{2} - 21\right), \\ \mathcal{G}_{R_Z} &= k\left(\frac{135n^2}{2} + \frac{105n}{2} - 21\right).\end{aligned}\quad (\text{B41})$$

*Proof.* By employing the spectral method, the 1D Lapla-

cian can be decomposed as [45]

$$L = \mathcal{F}^\dagger \cdot \Lambda \cdot \mathcal{F}, \quad (\text{B42})$$

where  $\mathcal{F}, \mathcal{F}^\dagger$  represent a Fourier pair and  $\Lambda$  is diagonal with phases determined by the spectrum.

Using [Lemma 9](#) and [Lemma 10](#) with the gate-set [Definition 4](#), a single implementation of  $L$  on  $n$  qubits requires QFT,  $\text{QFT}^\dagger$ , and the diagonal phase network, hence has gate count

$$\begin{aligned} \mathcal{G}_H &= 2n, \\ \mathcal{G}_{\text{CNOT}} &= 2n(n+1) + \frac{(n+1)(n-2)}{2}, \\ \mathcal{G}_{R_Z} &= 2n(n+1) + \frac{n(n-1)}{2}. \end{aligned} \quad (\text{B43})$$

For the 3D Laplacian  $A$  acting on  $3n$  qubits, applying the same construction to each spatial dimension yields with control by [Lemma 7](#) with [Lemma 9](#), [Lemma 10](#) and [Lemma 6](#) the per-application gate count

$$\begin{aligned} \mathcal{G}_H &= 15n^2 + 21n - 6, \\ \mathcal{G}_S &= 12n, \\ \mathcal{G}_{\text{CNOT}} &= \frac{135n^2}{2} + \frac{93n}{2} - 21, \\ \mathcal{G}_{R_Z} &= \frac{135n^2}{2} + \frac{105n}{2} - 21. \end{aligned} \quad (\text{B44})$$

Finally, to realize  $U^k$  in QPE one may implement  $U^k$  by  $k$  sequential applications of  $U$  (as discussed for the  $k = 2^j$  powers in [51]). Therefore each primitive gate count scales linearly in  $k$ , yielding the stated expressions.  $\square$

**Lemma 12** (Gate complexity of QPE). *Consider the gate complexity of QPE using controlled powers  $CU^{2^j}$  of a unitary  $U$  generated by the (3D) Laplacian defined by [Definition 5](#), on a partially-fault-tolerant quantum computer with architecture defined by [Definition 4](#). Assume that each controlled power  $CU^{2^j}$  is implemented by the spectral method for the Laplacian. Then the implementation requires a gate count*

$$\begin{aligned} \mathcal{G}_H &= n_\lambda (15n^2 + 21n - 6) + 2n_\lambda, \\ \mathcal{G}_S &= 12n n_\lambda, \\ \mathcal{G}_{\text{CNOT}} &= n_\lambda \left( \frac{135n^2}{2} + \frac{93n}{2} - 21 \right) + n_\lambda (n_\lambda + 1), \\ \mathcal{G}_{R_Z} &= n_\lambda \left( \frac{135n^2}{2} + \frac{105n}{2} - 21 \right) + n_\lambda (n_\lambda + 1). \end{aligned} \quad (\text{B45})$$

*Proof.* Standard QPE applies Hadamards on the  $n_\lambda$ -qubit eigenvalue register, then applies the controlled powers  $CU^{2^j}$  for  $0 \leq j < n_\lambda$ , and finally applies an inverse QFT on the eigenvalue register.

For the Laplacian simulation used here, the controlled

unitary  $CU$  is implemented by the spectral method, which diagonalizes the Laplacian in the Fourier basis. In particular, the circuit for  $CU$  consists of QFT and inverse-QFT blocks on the system register together with a diagonal phase network whose phases are determined by the Laplacian spectrum. Under this construction, replacing  $U$  by  $U^{2^j}$  amounts to multiplying the diagonal phases by  $2^j$ , while keeping the circuit structure unchanged. Therefore, each controlled power  $CU^{2^j}$  has the same STAR-gate counts as  $CU$  itself (up to the choice of rotation angles), and the gate cost per controlled power is the  $k = 1$  case of [Lemma 11](#). Since QPE uses  $n_\lambda$  controlled powers, the total contribution of the controlled- $U^{2^j}$  blocks is  $n_\lambda$  times the per-application cost from [Lemma 11](#) with  $k = 1$ .

The eigenvalue register contributes  $n_\lambda$  Hadamards at the start of QPE and an additional  $n_\lambda$  Hadamards from the inverse QFT. The inverse-QFT on the eigenvalue register also contributes  $n_\lambda(n_\lambda + 1)$  CNOT gates and  $n_\lambda(n_\lambda + 1)$   $R_Z$  gates by [Lemma 9](#). Summing these contributions yields the stated expressions.  $\square$

*c. Cost of eigenvalue inversion* We consider implementing the conditional rotation step of HHL, where after QPE one must apply a controlled  $R_Y$  rotation with angle

$$f(x) = \arcsin \left( \frac{c}{x} \right) \quad (\text{B46})$$

conditioned on the  $n_\lambda$ -qubit eigenvalue register (as in Sec. VI of [51]).

In the approximate (non-exact) reciprocal path, the breakpoints and polynomial degree are chosen as [51]

$$\begin{aligned} a &= (2^{n_\lambda})^{2/3}, \\ c &= \frac{2^{n_\lambda} t \lambda_{\min}}{2\pi}, \\ t &= 2\pi \cdot \frac{2^{n_\lambda} - 1}{2^{n_\lambda} \lambda_{\max}}, \\ r &= \frac{2c}{a} + \sqrt{\left| 1 - \left( \frac{2c}{a} \right)^2 \right|}, \\ d &= \left\lceil \log \left( 1 + \frac{16.23 \sqrt{\ln^2(r) + (\pi/2)^2} \kappa (2\kappa - \varepsilon)}{\varepsilon} \right) \right\rceil, \\ M &= \left\lceil \log_5 \left( \frac{2^{n_\lambda} - 1}{a} \right) \right\rceil. \end{aligned} \quad (\text{B47})$$

The resource estimate in Appendix B of [52] gives the following Toffoli count for the parallel piecewise-polynomial evaluation (labeling + parallel Horner evalu-

ation):

$$\begin{aligned} \mathcal{G}_{\text{Toff}} &= \frac{3}{2}n_\lambda^2d + 3n_\lambda pd + \frac{7}{2}n_\lambda d - \frac{3}{2}p^2d + 3pd - d \\ &+ 2Md\left(4d\lceil\log_2 M\rceil - 8\right) + 4Mn_\lambda. \end{aligned} \quad (\text{B48})$$

Using [Lemma 6](#), the Toffoli-dominated STAR-gate complexities of the arithmetic part of the conditioned-rotation step are

$$\begin{aligned} \mathcal{G}_H^{\text{inv}} &= 2\mathcal{G}_{\text{Toff}}, \\ \mathcal{G}_{\text{CNOT}}^{\text{inv}} &= 7\mathcal{G}_{\text{Toff}}, \\ \mathcal{G}_{R_Z}^{\text{inv}} &= 7\mathcal{G}_{\text{Toff}}, \\ \mathcal{G}_S^{\text{inv}} &= 0. \end{aligned} \quad (\text{B49})$$

*d. Overall analysis* We first define the single-shot cost of the HHL block  $\tilde{U}_{\text{HHL}}$  used inside amplitude amplification. In our Laplacian setting, the number of qubits needed to represent the eigenvalues to precision scales with the number of bits required to resolve eigenvalues down to  $\Theta(1/\kappa)$ . Accordingly, we set [\[51\]](#)

$$n_\lambda = 3 \left( \left\lceil \log \left( \frac{2(2\kappa^2 - \varepsilon)}{\varepsilon} + 1 \right) \right\rceil + 1 \right), \quad (\text{B50})$$

and treat  $n_\lambda$  as a derived parameter from  $\kappa$  in the final gate-count expressions.

**Definition 7** (Single-shot gate complexity of HHL). *Consider the HHL circuit  $\tilde{U}_{\text{HHL}}$  over the [Definition 4](#) gate set applied to the 3D Laplacian instance described by [Definition 2](#). Let  $n$  denote the per-dimension register size used by the Laplacian simulation in [Lemma 11–Lemma 12](#), let  $\kappa$  be the condition number, and set [\[51\]](#)*

$$n_\lambda = 3 \left( \left\lceil \log \left( \frac{2(2\kappa^2 - \varepsilon)}{\varepsilon} + 1 \right) \right\rceil + 1 \right). \quad (\text{B51})$$

Let  $m$  denote the truncation order of the Fourier series loader (FSL), and let  $\varepsilon$  be the tolerance parameter used in the eigenvalue-inversion step.

We define  $\tilde{U}_{\text{HHL}}$  to comprise state preparation (FSL), QPE, and the eigenvalue-dependent inversion/rotation gadget, but to exclude eigenvalue uncomputation (that is,  $\tilde{U}_{\text{HHL}}$  does not include  $\tilde{U}_{\text{QPE}}^\dagger$ ). Consequently, the system register may remain entangled with the eigenvalue register after applying  $\tilde{U}_{\text{HHL}}$ .

Define

$$T_{\text{inv}}(n_\lambda, \kappa, \varepsilon) := T(n_\lambda, d(n_\lambda, \kappa, \varepsilon), p, M(n_\lambda, \kappa, \varepsilon)), \quad (\text{B52})$$

where  $T_{\text{inv}}$  is the Toffoli-count expression in the eigenvalue-inversion paragraph and  $(d, p, M)$  are the associated piecewise-polynomial parameters. Then the STAR-gate complexity of a single application of  $\tilde{U}_{\text{HHL}}$

is defined by the sum of the three dominant blocks:

$$\begin{aligned} \mathcal{G}_H^{\text{HHL}}(n, \kappa, \varepsilon, m) &= \mathcal{G}_H^{\text{FSL}}(n, m) + \mathcal{G}_H^{\text{QPE}}(n, n_\lambda) \\ &+ \mathcal{G}_H^{\text{inv}}(n_\lambda, \kappa, \varepsilon), \\ \mathcal{G}_S^{\text{HHL}}(n, \kappa, \varepsilon, m) &= \mathcal{G}_S^{\text{FSL}}(n, m) + \mathcal{G}_S^{\text{QPE}}(n, n_\lambda) \\ &+ \mathcal{G}_S^{\text{inv}}(n_\lambda, \kappa, \varepsilon), \\ \mathcal{G}_{\text{CNOT}}^{\text{HHL}}(n, \kappa, \varepsilon, m) &= \mathcal{G}_{\text{CNOT}}^{\text{FSL}}(n, m) + \mathcal{G}_{\text{CNOT}}^{\text{QPE}}(n, n_\lambda) \\ &+ \mathcal{G}_{\text{CNOT}}^{\text{inv}}(n_\lambda, \kappa, \varepsilon), \\ \mathcal{G}_{R_Z}^{\text{HHL}}(n, \kappa, \varepsilon, m) &= \mathcal{G}_{R_Z}^{\text{FSL}}(n, m) + \mathcal{G}_{R_Z}^{\text{QPE}}(n, n_\lambda) \\ &+ \mathcal{G}_{R_Z}^{\text{inv}}(n_\lambda, \kappa, \varepsilon), \end{aligned} \quad (\text{B53})$$

where  $\mathcal{G}^{\text{QPE}}(n, n_\lambda)$  are the counts from [Lemma 12](#),  $\mathcal{G}^{\text{FSL}}(n, m)$  are the counts from the FSL paragraph, and

$$\begin{aligned} \mathcal{G}_H^{\text{inv}}(n_\lambda, \kappa, \varepsilon) &= 2T_{\text{inv}}(n_\lambda, \kappa, \varepsilon), \\ \mathcal{G}_{\text{CNOT}}^{\text{inv}}(n_\lambda, \kappa, \varepsilon) &= 7T_{\text{inv}}(n_\lambda, \kappa, \varepsilon), \\ \mathcal{G}_{R_Z}^{\text{inv}}(n_\lambda, \kappa, \varepsilon) &= 7T_{\text{inv}}(n_\lambda, \kappa, \varepsilon), \\ \mathcal{G}_S^{\text{inv}}(n_\lambda, \kappa, \varepsilon) &= 0. \end{aligned} \quad (\text{B54})$$

We next account for the gate complexity of the amplitude-amplification operator  $(U_s \tilde{U}_\omega)^k$  used in our construction. We first include the diffusion operator  $U_0$  shown in [FIG. 2](#). Its circuit realization requires a  $(3n + n_\lambda)$ -controlled  $X$  gate, together with  $2(3n + n_\lambda + 1)$   $X$  gates. Applying [Lemma 8](#) to decompose the multi-controlled  $X$  gate yields the total gate counts

$$\begin{aligned} \mathcal{G}_H^{U_0}(n, n_\lambda) &= 60n + 20n_\lambda - 90, \\ \mathcal{G}_S^{U_0}(n, n_\lambda) &= 12n + 4n_\lambda + 4, \\ \mathcal{G}_{\text{CNOT}}^{U_0}(n, n_\lambda) &= 168n + 56n_\lambda - 336, \\ \mathcal{G}_{R_Z}^{U_0}(n, n_\lambda) &= 168n + 56n_\lambda - 336. \end{aligned} \quad (\text{B55})$$

Here we used the identity  $X = HS^2H$  to express the  $2(3n + n_\lambda + 1)$   $X$  gates as Clifford gates only, and we introduced an additional pair of Hadamard gates for the target of the  $(3n + n_\lambda)$ -controlled  $X$  gate. We emphasize that no additional Hadamard gates are required outside the controlled operation, since the reflection is performed about

$$U_0 = \mathbb{I} - 2|0\rangle\langle 0|, \quad (\text{B56})$$

rather than about  $\mathbb{I} - 2|s\rangle\langle s|$  as in standard Grover diffusion with the uniform superposition  $|s\rangle$  [\[62\]](#).

We next consider the remaining components of the amplitude-amplification step. Implementing  $\tilde{U}_\omega$  requires two HHL blocks, namely  $(\tilde{U}_{\text{HHL}}, \tilde{U}_{\text{HHL}}^\dagger)$ . The phase oracle  $U_s$  contributes two  $S$  gates. Since  $\tilde{U}_{\text{HHL}}$  and  $\tilde{U}_{\text{QPE}}^\dagger$  have the same STAR-gate counts as their forward counterparts, we may express the per-iteration cost of  $U_s \tilde{U}_\omega$  in terms of the block costs already defined.

**Definition 8** (Gate complexity of HHL with amplitude amplification). *Adopt the setting and notation of Definition 7, with  $n_\lambda$  defined as in Definition 7 and truncation order  $m$  treated as an input. Amplitude amplification is performed on the joint system–eigenvalue Hilbert space, and no eigenvalue uncomputation is carried out within each iteration.*

Let the number of amplitude-amplification iterations be

$$k = \frac{\kappa}{1 - \varepsilon}. \quad (\text{B57})$$

The phase oracle  $U_s$  contributes two  $S$  gates and no Hadamard,  $CNOT$ , or  $R_Z$  gates.

Define the STAR-gate complexity of a single amplitude-amplification iteration  $U_s \tilde{U}_\omega$  by

$$\begin{aligned} \mathcal{G}_H^{iter}(n, \kappa, \varepsilon, m) &= 2\mathcal{G}_H^{HHL}(n, \kappa, \varepsilon, m) + \mathcal{G}_H^{U_0}(n, n_\lambda), \\ \mathcal{G}_S^{iter}(n, \kappa, \varepsilon, m) &= 2\mathcal{G}_S^{HHL}(n, \kappa, \varepsilon, m) + \mathcal{G}_S^{U_0}(n, n_\lambda) + \mathcal{G}_S^{U_s}, \\ \mathcal{G}_{CNOT}^{iter}(n, \kappa, \varepsilon, m) &= 2\mathcal{G}_{CNOT}^{HHL}(n, \kappa, \varepsilon, m) + \mathcal{G}_{CNOT}^{U_0}(n, n_\lambda), \\ \mathcal{G}_{R_Z}^{iter}(n, \kappa, \varepsilon, m) &= 2\mathcal{G}_{R_Z}^{HHL}(n, \kappa, \varepsilon, m) + \mathcal{G}_{R_Z}^{U_0}(n, n_\lambda), \end{aligned} \quad (\text{B58})$$

where  $\mathcal{G}_S^{U_s} = 2$ . Then the gate complexity of the HHL with amplitude-amplification operator  $(U_s \tilde{U}_\omega)^k$  is

$$k\mathcal{G}^{iter}(n, \kappa, \varepsilon, m). \quad (\text{B59})$$

If a clean solution state in the system register is required at the end of the algorithm, a single inverse QPE block  $\tilde{U}_{QPE}^\dagger$  may be applied once after the amplification step, contributing an additional  $\mathcal{G}^{QPE}(n, n_\lambda)$  to the total gate complexity.

### Appendix C: Supplementary information

This supplementary information provides additional analyses and supporting evidence for the scaling behavior and resource estimates discussed in the main text. We focus on clarifying the mechanisms underlying the runtime improvement of QACG relative to classical CG and full HHL, with particular emphasis on the role of condition-number reduction, quantum error-correction (QEC) cycle time, and eigenvalue-inversion overheads. The figures in this section examine, in turn, (i) the dependence of HHL runtime on the effective quantum condition number, (ii) the redistribution of conditioning between quantum and classical stages in runtime-optimized QACG, and (iii) the scaling of key parameters governing the eigenvalue inversion subroutine. Together, these results provide a detailed, quantitative foundation for interpreting the crossover behavior and architectural trade-offs reported in the main text.

In FIG. 9, we estimate the expected runtime of HHL for the 3D Poisson equation under different assumptions on the quantum condition number  $\kappa'$  and the QEC cy-

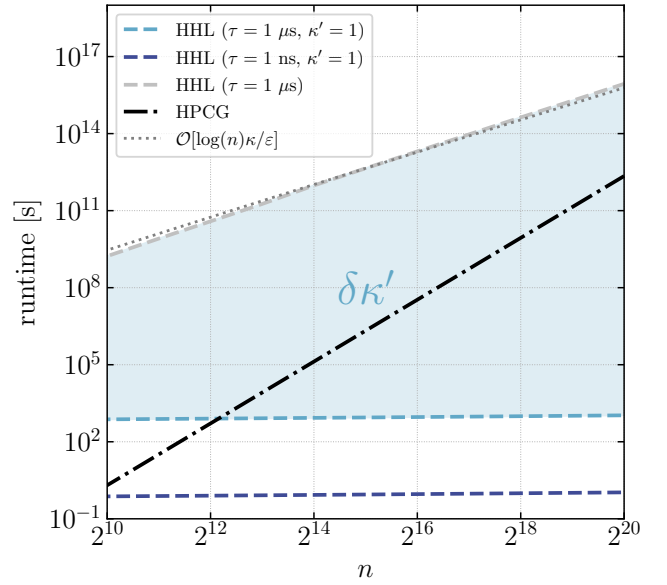


FIG. 9. Estimated HHL runtimes for the 3D Poisson equation under different assumptions on the QEC cycle time  $\tau$  and the quantum condition number  $\kappa'$ . The dotted reference curve indicates the scaling  $\mathcal{O}[\log(n)\kappa/\varepsilon]$  for comparison. Restricting the effective condition number handled by the quantum subroutine reduces the explicit  $\kappa$ -dependence, leading to a markedly reduced scaling slope with respect to  $n$ . When  $\kappa'$  is held constant, the resulting runtime exhibits an exponential separation from the HHL, while faster QEC cycles shift the crossover to smaller problem sizes without altering the asymptotic scaling.

cle time  $\tau$ . The horizontal axis denotes the number of unknowns per spatial dimension  $n$ , while the vertical axis shows the estimated runtime in seconds. The dash-dotted black curve represents the benchmark-calibrated classical HPCG baseline.

The dashed gray curve corresponds to HHL with  $\tau = 1, \mu\text{s}$  and  $\kappa' = \kappa$ , where the quantum subroutine must resolve the full condition number of the linear system. In this case, the runtime follows a steep dependence on  $n$ , reflecting the scaling  $\kappa = \mathcal{O}(n^2)$  for the 3D Poisson operator (Lemma 3), together with the reference complexity  $\mathcal{O}[\log(n)\kappa/\varepsilon]$  for HHL.

By contrast, the dashed light-blue and dark-blue curves show HHL with the quantum condition number restricted to  $\kappa' = 1$ , for  $\tau = 1, \mu\text{s}$  and  $\tau = 1, \text{ns}$ , respectively. In this regime, the explicit  $\kappa$ -dependence is removed from the quantum stage, leaving only a logarithmic dependence on  $n$ . As a result, replacing  $\kappa = \mathcal{O}(n^2)$  by a constant yields an exponential separation in runtime relative to the classical baseline as  $n$  increases. This corrected plot therefore makes explicit that the dominant mechanism for runtime improvement in QACG is the reduction of the condition number handled by the quantum subroutine, rather than the absolute speed of quantum gates alone. Faster QEC cycles act multiplicatively,

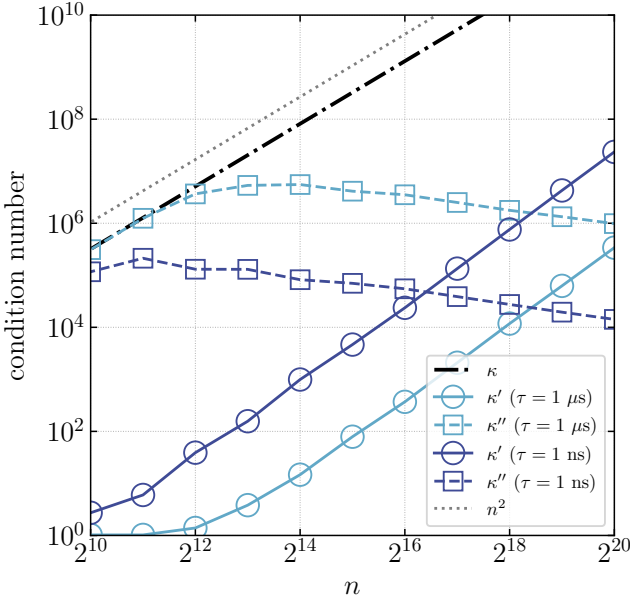


FIG. 10. Scaling of the full condition number  $\kappa$ , the optimized quantum condition number  $\kappa'$ , and the effective classical condition number  $\kappa''$  for runtime-optimized QACG as a function of problem size  $n$ . The dotted curve indicates the reference scaling  $\kappa = \mathcal{O}(n^2)$  for the 3D Poisson equation.

shifting the crossover to smaller problem sizes without changing the asymptotic slope.

FIG. 10 shows how the condition numbers entering QACG evolve with the problem size  $n$ . The solid black curve indicates the full condition number  $\kappa$ , which scales as  $\mathcal{O}(n^2)$  for the Poisson operator. The colored curves show the runtime-optimized quantum condition number  $\kappa'$  and the corresponding effective classical condition number  $\kappa''$  for  $\tau = 1, \mu\text{s}$  and  $\tau = 1, \text{ns}$ .

For small  $n$ , the optimized  $\kappa'$  remains close to unity,

indicating that only a very narrow low-energy spectral band is treated quantum mechanically. In this regime, QACG behaves similarly to classical CG, whose complexity benefits from the  $\sqrt{\kappa}$  dependence of convergence. As  $n$  increases, however,  $\kappa'$  grows steadily, reflecting the increasing benefit of initializing a broader low-energy subspace on the quantum processor. This growth marks the crossover region in which the logarithmic dependence on  $n$  inherent to HHL becomes advantageous relative to the  $\sqrt{\kappa}$  scaling of CG.

Correspondingly, the effective classical condition number  $\kappa''$  decreases as  $\kappa'$  increases, indicating that the slowest classical error modes are progressively removed by the quantum initialization. The separation between  $\kappa'$  and  $\kappa''$  thus quantifies the redistribution of conditioning between quantum and classical resources, and explains the emergence of a runtime advantage for QACG at large problem sizes.

FIG. 11 presents the scaling of the parameters used in the eigenvalue inversion subroutine of HHL. The observed trends are consistent with their definitions in App. B. In particular, the scaling of  $a$ ,  $c$ , and  $r$  reflects their explicit dependence on the spectral bounds of the Poisson operator, while the decrease in  $t$  with increasing  $n$  compensates for the growth of the maximum eigenvalue.

The polynomial degree  $d$  grows moderately with  $n$ , consistent with the increasing precision required to approximate the inverse over a widening spectral range. The parallelization factor  $M$  also increases slowly, reflecting the logarithmic dependence on the inverse error tolerance. Importantly, the figure illustrates that the product  $d, n_\lambda$  constitutes a dominant contribution to the space complexity of the parallel piecewise-polynomial evaluation used for eigenvalue inversion. This behavior explains why, despite substantial reductions in gate counts, the logical qubit requirement remains significant, as discussed in the resource-estimation analysis.

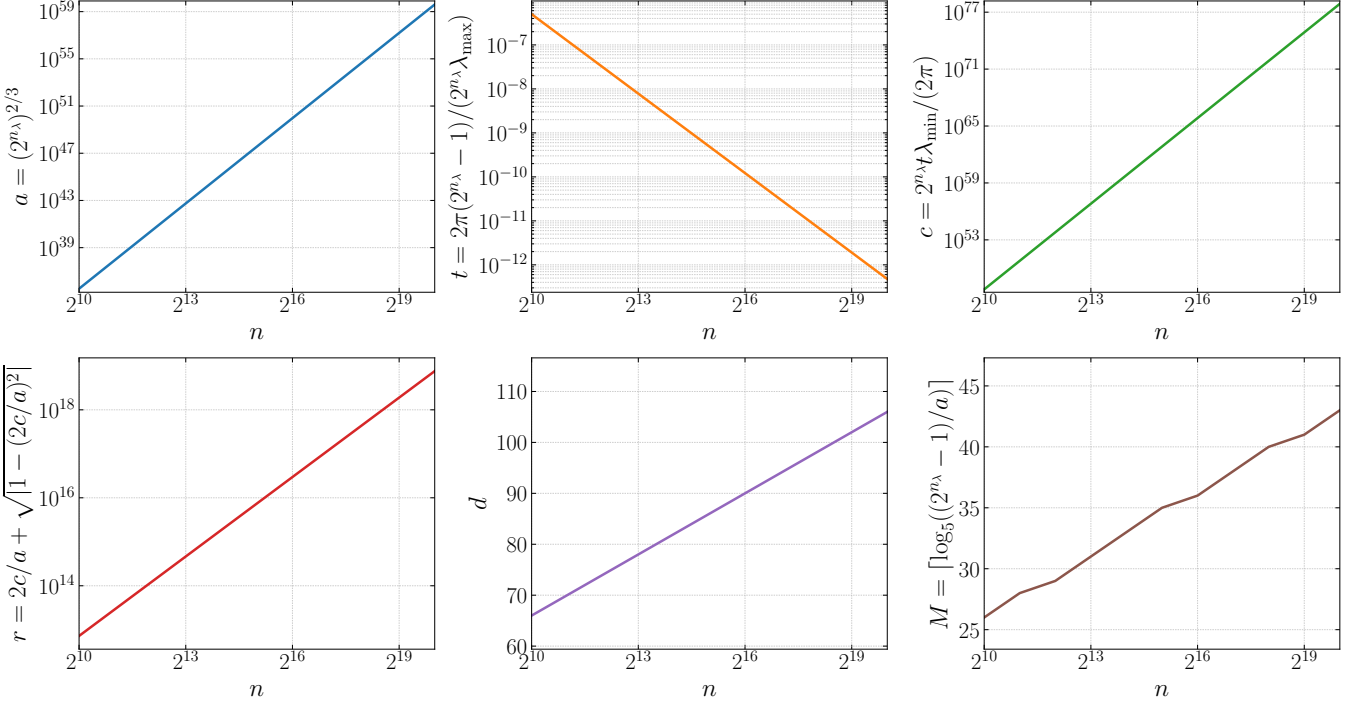


FIG. 11. Scaling of the parameters entering the eigenvalue inversion subroutine as a function of  $n$ : the scaling factor  $a$ , evolution time  $t$ , resolution scale of QPE  $c$ , spectral compression factor  $r$ , polynomial degree  $d$ , and piecewise factor  $M$ .